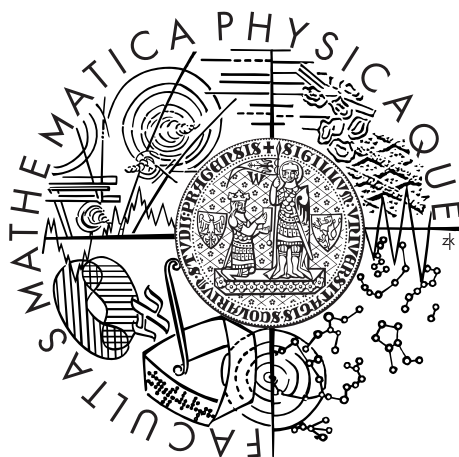


Charles University in Prague  
Faculty of Mathematics and Physics

## MASTER THESIS



Jan Blechta

## Matematické modelování růstu krystalů

### Mathematical modeling of crystal growth

Mathematical Institute of Charles University

Supervisor of the master thesis: Jaroslav Hron

Study programme: Physics

Specialization: Mathematical and Computer  
Modelling in Physics  
and Engineering

Prague 2013

# Acknowledgements

First of all, I would like to thank Prof. Josef Málek for inspiring consultations but more importantly for the enthusiasm he gives to people collaborating with. Special thanks to Dr. Ondřej Souček for very helpful discussions about problems of continuum thermomechanics. I am also very grateful to both Ondřej and Prof. Málek for lectures they conduct which led me on the long way of getting understand basics of PDEs and multi-phase thermomechanics.

My thanks belong also to Robert Král for initiating me into the mysteries of crystal growth and for supplying me with many material data and experimental data of temperature measurements.

Whole crew of FEniCS project deserves appreciation for the great job they do. I especially thank to Prof. Anders Logg, Prof. Garth N. Wells and Dr. Johan Hake for their responsiveness and cooperability on fixing bugs and implementing some minor features we needed.

Last but not least, I thank Dr. Jaroslav Hron for not only supervising this work but also for valuable hints in numerics and programming. Generally, I also appreciate much his occupation on administration of the Karlín cluster.

I declare that I carried out this master thesis independently, and only with the cited sources, literature and other professional sources.

I understand that my work relates to the rights and obligations under the Act No. 121/2000 Coll., the Copyright Act, as amended, in particular the fact that the Charles University in Prague has the right to conclude a license agreement on the use of this work as a school work pursuant to Section 60 paragraph 1 of the Copyright Act.

In Prague on August 2, 2013

Název práce: Matematické modelování růstu krystalů

Autor: Jan Blechta

Katedra: Matematický ústav UK

Vedoucí diplomové práce: RNDr. Ing. Jaroslav Hron, Ph.D.

Abstrakt: Předkládáme model Bridgmanova růstu krystalu. Pseudonestlačitelná podmínka je použita vzhledem k skoku hustoty při fázové změně. ALE formulace je využita k popisu pohyblivých částí systému. Polní rovnice a posunutí materiálových rozhraní jsou řešeny separátně. Naviér-Stokesův problém je rozšířen do krystalické fáze a klid je vynucen penaltou podobnou Darcyho zákonu. Latentní teplo krystalizace je vyjádřeno aproximací Diracovy distribuce a přidáno k efektivní tepelné kapacitě. Implicitní Eulerova diskretizace je použita v čase a P2/P1/P1 elementy v prostoru. Stacionární i nestacionární řešení jsou počítána a porovnávána s experimentálními teplotními daty měřenými uvnitř systému ve stacionárním stavu. Vliv rychlostí tažení na proces růstu je zkoumána a tvar fázového rozhraní je vyhodnocen.

Klíčová slova: růst krystalu, fázový přechod, proudění, pseudonestlačitelnost

Title: Mathematical modeling of crystal growth

Author: Jan Blechta

Department: Mathematical Institute of Charles University

Supervisor: RNDr. Ing. Jaroslav Hron, Ph.D.

Abstract: We present a numerical model of Bridgman crystal growth. Pseudo-incompressibility constraint is used to handle jumps in density during phase change. ALE formulation is employed to account for moving parts of the system. Field equations and movement of material interfaces are decoupled in fractional step manner. Naviér-Stokes problem is extended to solid phase where no flow is enforced by Darcy-like forcing. Latent heat of phase change is added to effective heat capacity as approximate Dirac- $\delta$ . Backward Euler discretization in space and P2/P1/P1 in space are used. Transient and stationary solutions are being found and compared to temperatures measured directly inside a steady system. Influence of pull-rates on growth process and shape of phase interface are being examined.

Keywords: crystal growth, phase-change, flow, pseudo-incompressibility

# Contents

<b>Introduction</b>	<b>2</b>
<b>1 Crystal growth by vertical Bridgman method</b>	<b>3</b>
1.1 Introduction to Bridgman method . . . . .	3
1.2 Properties of lead chloride . . . . .	3
1.3 Experimental arrangement . . . . .	4
<b>2 Mathematical model</b>	<b>7</b>
2.1 Balance equations . . . . .	8
2.1.1 Energy balance . . . . .	8
2.1.2 Balance of linear momentum . . . . .	10
2.1.3 Mass balance . . . . .	11
2.1.4 Complete model . . . . .	14
2.2 Weak form of equations . . . . .	16
2.3 Cylindrical coordinates . . . . .	19
2.4 Notes on Allen-Cahn type model . . . . .	21
2.4.1 Classical thermodynamics of interface . . . . .	21
2.4.2 Diffuse interface thermodynamics . . . . .	22
<b>3 Numerical algorithm</b>	<b>25</b>
3.1 Arbitrary Lagrangian–Eulerian formulation . . . . .	26
3.2 Spatial discretization . . . . .	27
3.3 Temporal discretization . . . . .	28
3.4 Mesh . . . . .	30
3.5 Solution of field equations . . . . .	32
<b>4 Results</b>	<b>33</b>
4.1 Shape of phase interface . . . . .	35
4.2 Comparison with steady states . . . . .	39
4.3 Comparison with experimental data . . . . .	43
<b>Conclusion</b>	<b>49</b>
<b>Bibliography</b>	<b>50</b>
<b>List of tables</b>	<b>54</b>
<b>List of abbreviations and symbols</b>	<b>55</b>

# Introduction

The goal of this work is to propose and implement a numerical model which could predict temperature field, melt flow and a position and a shape of the the crystal/melt interface in the Bridgman experimental arrangement. In particular model is aimed to Bridgman growth of lead halides and ternary alkali lead halides in specific laboratory conditions, i.e. particular experimental procedure, geometry and material properties of apparatus.

Growth of high-quality single crystals is sensitive to conditions being enforced during growth process. Experimental optimization of relevant conditions is lengthy and time-consuming process. For our specific problem of a growth of single crystal of  $\text{PbCl}_2$  of weight ca. 150 g, the growth itself lasts few days. There are plenty of parameters to be set and numerical modeling can help with this issue.

Modeling and numerical realization of crystal growth problems represents challenging task. Model must be able to handle a phase change from a liquid phase to a solid phase – i.e. phases of which behaviour is qualitatively different. There are few conceptually different classes of models for description of phase changes. Some of them are well-established but other are still subject to current research, regarding their mathematical but also thermodynamical aspects.

Real solid–liquid phase changes possesses significant jump in material density. This has non-trivial consequences and plenty of models incorporates simplifying assumptions being in contradiction with these consequences. We will try to incorporate this density jump to the model.

Crystal growth modeling potentially incorporates many different phenomena driving a process. Things are getting very complicated when dealing with a material of two and more chemical substances. Luckily we will avoid this.

Another complication is movement present in a growth system. This puts non-trivially increased computational effort to many numerical methods in comparison to problems with static domains. We will use finite element method (FEM) to discretization of the problem as this is method suitable for solving problem in complicated geometries. We can then track moving structures of the system by fitted mesh although we will not particularly fit a mesh to evolving phase interface but use rather a different method.

We will take advantage of having available detailed description of the working crystal growth apparatus. Hence we are aware that we are trying to model real physical problem and take advantage of having opportunity to observe what is the real behaviour and what is not. Moreover some precise measurements were performed on the system of the concern which will enable us to compare modeled result directly to behaviour of the considered system.

# 1. Crystal growth by vertical Bridgman method

## 1.1 Introduction to Bridgman method

Vertical Bridgman method is a widely used technique for crystal growth of different materials from a melt.

During this procedure melted material within an ampoule is slowly pulled down through temperature gradient in a furnace. Temperature conditions in a furnace and a pulling rate are specifically chosen to achieve a development of high quality single crystal. In particular homogeneous nucleation in the bulk of melt needs to be avoided and convex or planar (see figure 1.1) crystal/melt interface is desirable to avoid formation of various crystal defects. Moreover some degree of melt stirring by natural convection is usually desirable to homogenize impurities and/or additives.

Typical schematic configuration of the setup is shown in figure 1.2. For more details regarding the Bridgman growth reader is referred to [12].

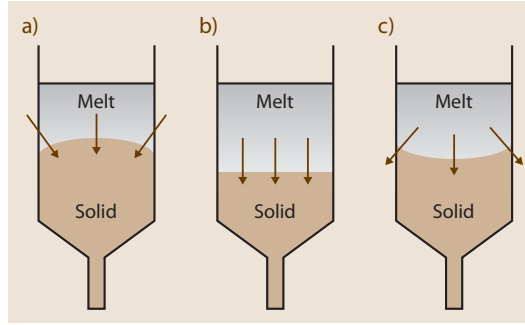


Figure 1.1: Crystal/melt interface shapes: (a) convex, (b) planar and (c) concave. Taken from [12, chapter 10] with kind permission of Springer Science+Business Media.

## 1.2 Properties of lead chloride

Lead(II) chloride ( $\text{PbCl}_2$ ) was chosen as a model compound for its availability in high purity, for widely available material coefficients and their temperature dependences, and similarity of its properties with ternary alkali lead halides (TALH) [20]. Lead halides [7] and TALH [28] are considered to be suitable as a low phonon host for rare earth (RE) doping and thus for construction of mid-infrared solid-state lasers [28, 17, 30]. Analysis – both experimental and theoretical – of ternary compounds growth is much more complicated by dependence of phase-equilibrium temperature on the phase fractions of components as is typically demonstrated by phase diagrams.

Crystalline lead chloride shows a slight anisotropy, as the most of crystals. In particular it has an orthorhombic bipyramidal structure. Dependence of material coefficients on crystallographic orientation is rarely available. We will use only isotropic coefficients and model will not show anisotropy at all. Anyway it is

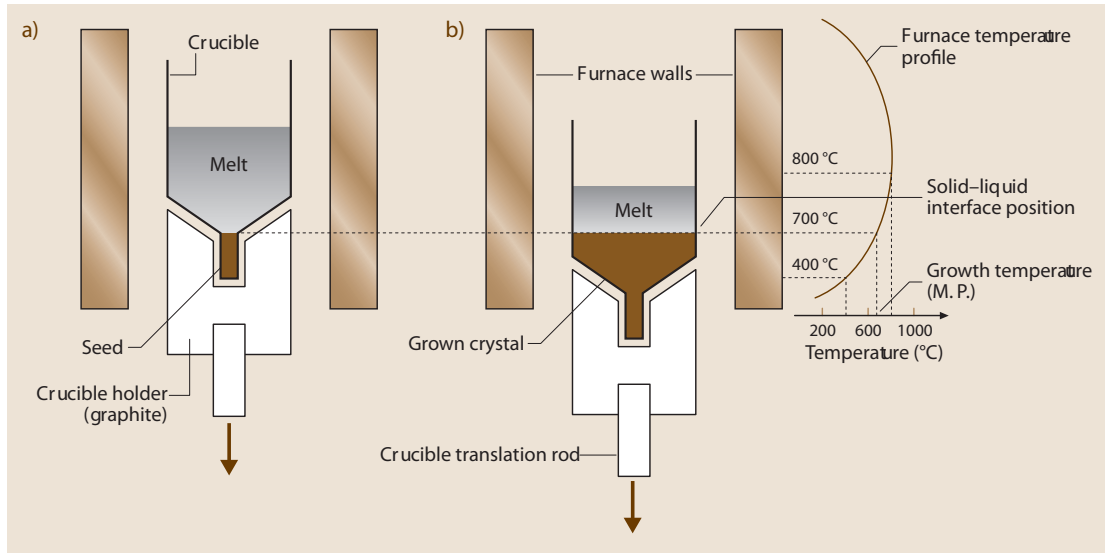


Figure 1.2: Schematic diagram of a vertical Bridgman crystal growth process in a single-zone furnace: (a) at the beginning of the experiment and (b) with partially grown crystal.

*Taken from [12, chapter 10] with kind permission of Springer Science+Business Media.*

hardly a drawback because growth method which will be described below does not permit a set-up of crystallographic orientation.

### 1.3 Experimental arrangement

All relevant parts of the used apparatus – i.e. ampoule (crucible), its holder and furnace – possess cylindrical symmetry. This will enable us to simplify computations to two dimensions which will lead to significantly less computational effort needed. This simplification would not be justifiable if turbulence occurred – precisely said, turbulent velocity and temperature fields could not be considered possessing cylindrical symmetry but only some statistical means of them could be.

Furnace has five independent unequal-sized heating zones. This allows setting a broad class of temperature profiles. This is done by setting constant current through resistance heating zones. Measured temperature profiles are displayed in figure 1.3 and the details of these measurements is described by Král in [20]. Temperature profiles are practically independent of the ampoule position and the fraction of solidified material. In other words, heat conditions in the system have almost no influence on temperature of furnace.

Ampoule is made of fused quartz. Major part (cca 2/3) of the ampoule is filled with high-purity  $\text{PbCl}_2$  and sealed. This procedure is performed under introduction of chlorination agent into the  $\text{PbCl}_2$  melt as described by Nitsch [27]. During growth process top part of the ampoule has temperatures from 500 to 585°C<sup>1</sup>. Therefore there is pressure slightly lower than standard atmospheric pressure in the ampoule atmosphere, particularly cca 0.8–0.9 bar.

<sup>1</sup>this is maximal temperature of used temperature profiles.



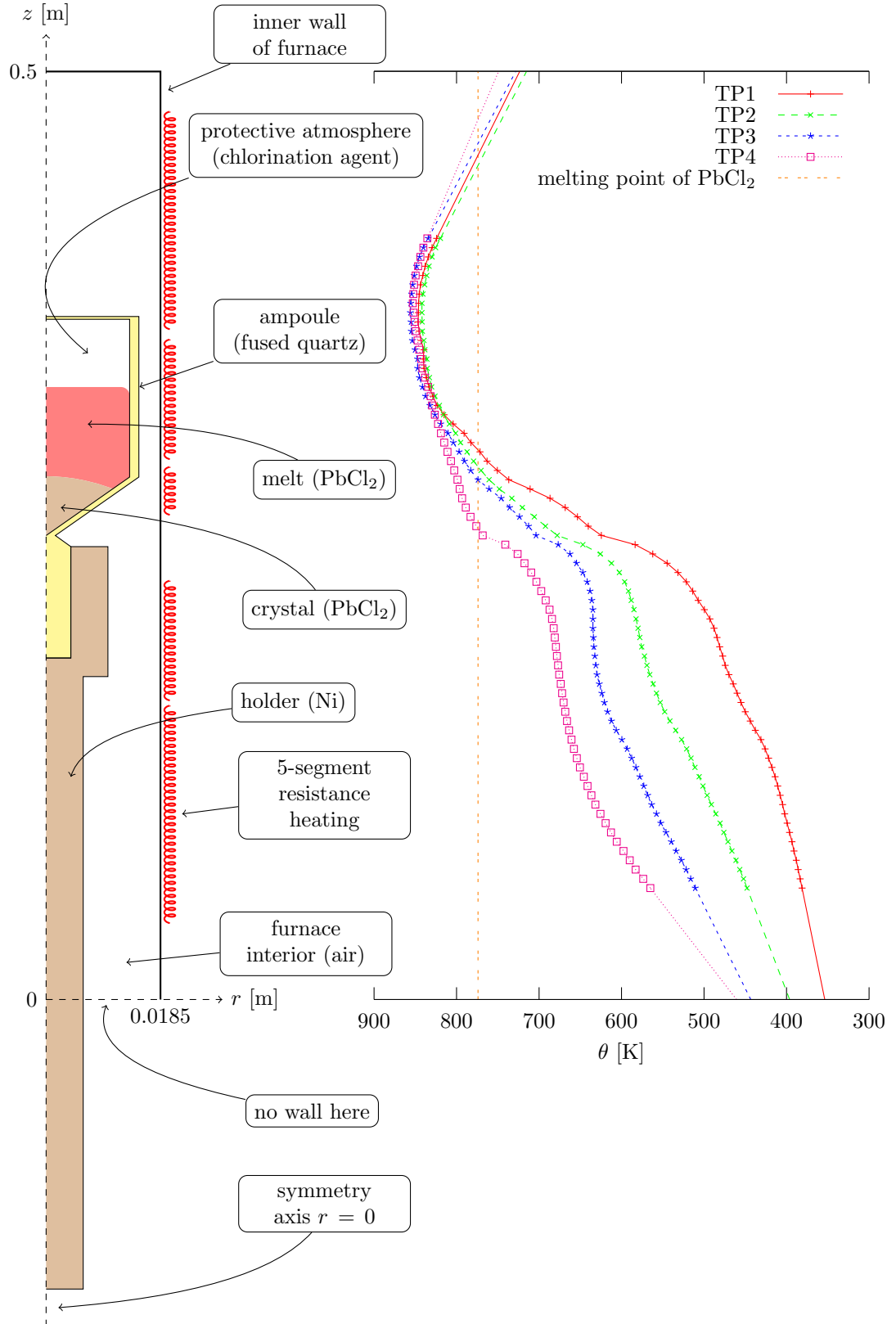


Figure 1.3: Scaled layout of used Bridgman apparatus. Aspect ratio is not preserved. Only half-section is shown – cylindrical symmetry applies. On the right, four temperature profiles at the inner wall of furnace are shown. Points are measured values and lines are linear extrapolation from two outer values.

Usual pulling rates range from 0.5 mm/h to 3 mm/h. This means that a growth process itself takes several days.

Apart from actual growth experiments, also temperature measurement experiments were designed and performed by Král [20]. These were done using special ampoule with capillaries for insertion of thermocouples which is depicted in figure 1.4. Steady state with fixed position of ampoule was reached and then measurement of temperature was performed throughout whole length of capillaries with step 1 mm. This was repeated with different positions of ampoule – i.e. different fractions of solidified substance – and with different temperature profiles.

These capillaries breaks cylindrical symmetry of the system. They may imply substantial differences of velocity field in comparison to proper ampoule, at least from kinematic reasons, but one may hope that they do not significantly disturb heat balance. We will discuss this more in chapter 4.

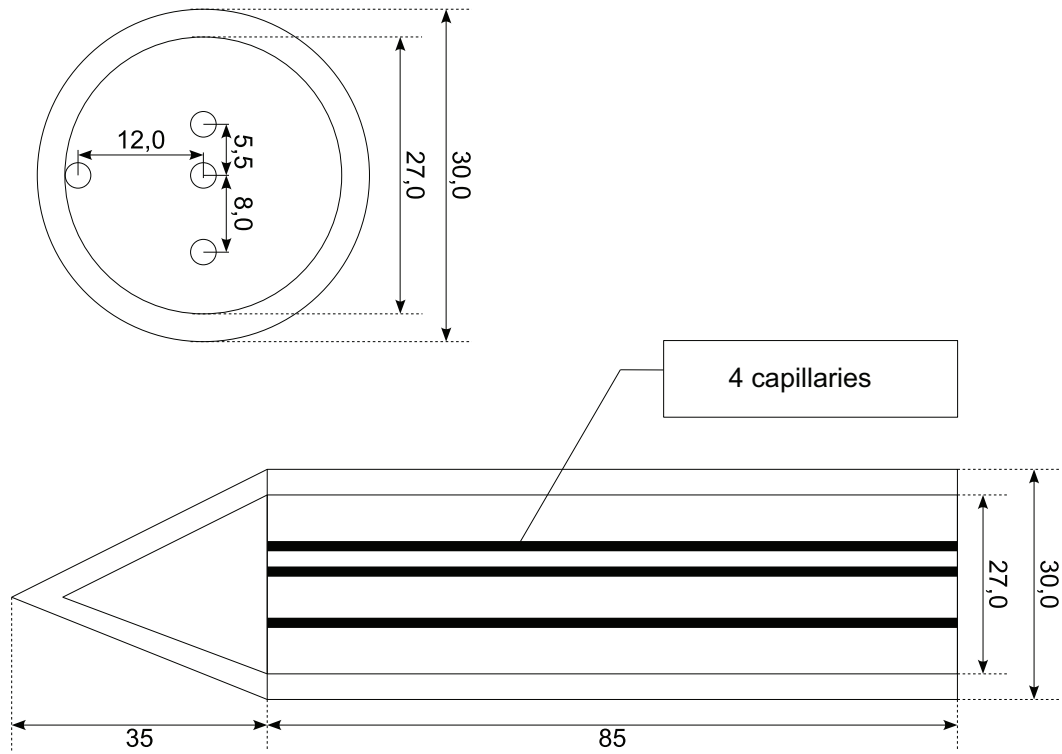


Figure 1.4: Geometry of ampoule with capillaries for temperature measurements. Dimensions are in millimetres.

*Figure by R. Král. Used with kind permission of the author.*

## 2. Mathematical model

There are plenty of physical phenomena driving crystal growth process described in previous chapter. Leaving microscopic structure of phase interface out of account we may try to model growth process in a framework of continuum thermomechanics. Evolution of phase interface is basically given by heat transfer – rate of heat drain controls the speed of crystallization. Therefore accurate description of concerning system must account for all significant heat transfer mechanisms if possible. Most important ones are

- conduction
- convection in fluid parts of system
- release of latent heat due to crystallization
- radiation<sup>1</sup>

There are also other effects of minor importance – one being buoyancy-induced diffusion of species in a melt giving raise to its non-homogeneity; this would be of much larger significance in binary and higher order substances. Viscous heating is other minor effect – in fact negligible how we will show in chapter 4.

Description of the interface between crystal and its melt is the most challenging part of the mathematical model and its numerical implementation also. For the main reasons we can count the facts that interface is not planar, its position is a priori unknown and evolving and the fact that there is fluid on one side and solid on the other side. On the other hand handling an interface with such a low curvature is much simpler than in the case of dendritic solidification.

Probably the oldest numerically realizable class of methods for solidification with moving interface are based on a quite heuristic modification of governing equations of fluid in way that solid behaviour is fulfilled in a part of the substance. This can be realized by either very high viscosity enforcing no flow [14] or by a momentum forcing in a fashion of Darcy’s law with very low permeability [26]. For an overview of methods of this kind reader is referred to [42]. In this work we adopted the latter approach. We can count these methods into class of diffuse-interface models.

Nowadays there is being performed active research of diffuse-interface models, also called phase-field models. One class of them originate in legendary works of Allen, Cahn and Hilliard [2, 8]. These were originally proposed for modeling surface effects between phases. Now the way how to fit these models into framework of continuum thermodynamics is subject of current research – see for instance Heida, Málek and Rajagopal [15, 16] or Aland and Voigt [1]. These models are able to describe a broader class of phenomena like supercooling/superheating. This is facilitated by penalizing a newly arising phase by a surface tension in a combination with a kinetic character of phase change mechanism. This advantage is naturally balanced by a need to prescribe more material quantities, constitutive relations and boundary conditions.

---

<sup>1</sup>We did not go into modeling the radiation as it is not of such an importance as for substances with much larger melting points.

Another possibility for a treatment of evolving phase interface is in using sharp interface approach. Balance equations describing each phase are enforced in respective regions. They share a common boundary constituting a sharp interface where a surface form of balance equations is being enforced. This approach generally has a pretty straightforward physical interpretation. It is distinguished by a sharp interface and well-separated pure phases. It may include various sort of interfacial constitutive relations, either equilibrium-like (e.g. temperature continuity) or kinetic (e.g. temperature jump proportional to heat flux). Šilhavý gives very exhausting and mathematically rigorous treatment of this topic (among others) in monograph [41]. On the other hand numerical treatment of sharp-interface models is much more challenging task and may possibly be accomplished by XFEM/PUM (extended finite element method/partition of unity method) – see [25, 10, 19].

In following sections we will describe details of the used model. We will also comment on Allen-Cahn type model a bit further.

## 2.1 Balance equations

We start with equations for mass, linear momentum and internal energy of single-component media

$$\dot{\rho} = -\rho \operatorname{div} \mathbf{u} \quad (2.1)$$

$$\rho \dot{\mathbf{u}} = \operatorname{div} \mathbf{T} + \rho \mathbf{b} \quad (2.2)$$

$$\rho \dot{e} = \mathbf{T} \cdot \nabla \mathbf{u} - \operatorname{div} \mathbf{q} \quad (2.3)$$

where  $\rho$  is density,  $\mathbf{u}$  velocity,  $\mathbf{T}$  Cauchy stress,  $\mathbf{b}$  mass-specific body force,  $e$  internal energy and  $\mathbf{q}$  heat flux. Dot above quantity denotes material derivative,  $\operatorname{div}$  is divergence operator and  $\nabla$  gradient operator.

Now we proceed by specifying constitutive relations and boundary or interfacial conditions we will use. We shall deal with balance equations applying to each part of the system separately. Multiple phases will be treated although this will apply only to  $\text{PbCl}_2$ . Other parts of the system (inert atmosphere, ampoule, air, holder) will be subject to same equations – while forgetting phase-change terms and possessing another material coefficients – and interfacial conditions coupling them will be given later.

### 2.1.1 Energy balance

Let's assume we can split Cauchy stress  $\mathbf{T}$  into isotropic equilibrium part given by thermodynamic pressure and dissipative part  $\mathbf{S}$  so that we have

$$\mathbf{T} = -p\mathbf{I} + \mathbf{S}. \quad (2.4)$$

Substituting this into balance of energy (2.3) and using balance of mass (2.1) we arrive at

$$\rho(\dot{e} + p\dot{\nu}) = \mathbf{S} \cdot \nabla \mathbf{u} - \operatorname{div} \mathbf{q} \quad (2.5)$$

where we introduced mass-specific volume  $\nu = 1/\rho$ . Introducing enthalpy  $h = e + p\nu$  we obtain enthalpy balance

$$\rho \dot{h} - \dot{p} = \mathbf{S} \cdot \nabla \mathbf{u} - \operatorname{div} \mathbf{q}. \quad (2.6)$$

Now consider material subject to phase transition whose phase is picked by value of quantity – so called phase-field  $0 \leq c \leq 1$ . We prescribe its energy by the classical Gibbs relation

$$\dot{e} = \theta \dot{\eta} - p \dot{\nu} + \mu \dot{c} \quad (2.7)$$

where  $\eta$  is entropy and  $\mu$  chemical potential. Using definition of enthalpy we rewrite this into

$$\dot{h} = \theta \dot{\eta} + \nu \dot{p} + \mu \dot{c}. \quad (2.8)$$

Now we define heat capacity at constant pressure  $c_p$ , latent heat of phase transition  $L$  and coefficient of thermal expansion  $\alpha$  as usual<sup>2</sup>

$$c_p = \left( \frac{\partial h}{\partial \theta} \right)_{p,c}, \quad (2.9)$$

$$L = \left( \frac{\partial h}{\partial c} \right)_{p,\theta}, \quad (2.10)$$

$$\alpha = \frac{1}{\nu} \left( \frac{\partial \nu}{\partial \theta} \right)_{p,c} = -\frac{1}{\nu} \left( \frac{\partial \eta}{\partial p} \right)_{\theta,c}. \quad (2.11)$$

Transforming enthalpy (2.8) from its natural variables  $\eta, p, c$  into variables  $p, \theta, c$  and using definitions (2.9)–(2.11) we obtain

$$\dot{h} = \nu(1 - \alpha\theta)\dot{p} + c_p\dot{\theta} + L\dot{c}. \quad (2.12)$$

Sticking this into enthalpy balance (2.6) we have

$$\rho c_p \dot{\theta} + \rho L \dot{c} - \alpha \theta \dot{p} = \mathbf{S} \cdot \nabla \mathbf{u} - \operatorname{div} \mathbf{q}. \quad (2.13)$$

This is useful form of energy balance in many practical situations when deformation contributes to pressure by negligible amount compared to external constraints so that pressure is practically constant<sup>3</sup> (e.g. at value of ambient pressure). We assume such a situation so we can neglect pressure term and consider remaining coefficients as a function of  $\theta$  and  $c$  only:

$$\rho(\theta, c) c_p(\theta, c) \dot{\theta} + \rho(\theta, c) L(\theta, c) \dot{c} = \mathbf{S} \cdot \nabla \mathbf{u} - \operatorname{div} \mathbf{q}. \quad (2.14)$$

We now focus on the phase change of our interest. We will assume that crystallization of  $\text{PbCl}_2$  in our crystal growth apparatus occurs at narrow interval  $(\theta_m - \epsilon, \theta_m + \epsilon)$  around equilibrium melting temperature  $\theta_m$ <sup>4</sup> so that phase-field  $c$  is for  $\epsilon > 0$  continuous function

$$c = c(\theta) \quad (2.15)$$

---

<sup>2</sup>Last equality in (2.11) is due to one of the Maxwell relations and is a statement of the integrability of the Gibbs potential  $g = e + p\nu - \theta\eta$ .

<sup>3</sup>Regarding motion of fluid this holds for low Mach number flows which are by the way approximately isochoric. Here we also clearly showed why in such a situation heat coefficient at constant pressure  $c_p$  should be used when expressing energy in the means of temperature rather than coefficient at constant volume  $c_\nu$ . For the physical reasoning one should take into consideration that even that flow is nearly isochoric so one would be tempted to use coefficient at constant volume  $c_\nu$ , actual external constraint on the motion is given by holding pressure – not volume – constant. Surroundings of the body do not perform an extra work  $(c_p - c_\nu)\dot{\theta}$  to keep the body at constant volume – this is only the *approximate* property of the motion.

<sup>4</sup>This assumption should quite precisely hold for our use case when the crystal grows slowly and with small curvatures of the phase interface. On the other hand it was observed by Král

meeting

$$c(\theta) = \begin{cases} 0 & \theta < \theta_m - \epsilon \\ 1 & \theta > \theta_m + \epsilon \end{cases}. \quad (2.16)$$

Having this in mind (2.14) takes form

$$\rho(\theta)c_p^{\text{eff}}(\theta)\dot{\theta} = \mathbf{S} \cdot \nabla \mathbf{u} - \text{div } \mathbf{q} \quad (2.17)$$

where we define

$$\rho(\theta) = \rho(\theta, c(\theta)), \quad (2.18)$$

$$c_p^{\text{eff}}(\theta) = c_p(\theta, c(\theta)) + L(\theta, c(\theta)) \frac{dc(\theta)}{d\theta}. \quad (2.19)$$

We observe that  $c(\theta)$  and  $dc(\theta)/dc$  are approximations of Heaviside function and Dirac distribution respectively, converging in the sense of distributions when  $\epsilon \rightarrow 0$ .

Next we neglect viscous heating in fluid parts (and stress work at all in solid parts) of the system so that first term on the right-hand side of (2.17) vanishes. Heat flux can be modeled by Fourier's law  $\mathbf{q} = -\kappa(\theta, c)\nabla\theta$ . Defining

$$\kappa(\theta) = \kappa(\theta, c(\theta)) \quad (2.20)$$

we finally arrive at heat equation

$$\rho(\theta)c_p^{\text{eff}}(\theta)\dot{\theta} = \text{div}(\kappa(\theta)\nabla\theta). \quad (2.21)$$

### 2.1.2 Balance of linear momentum

We have no intention to solve for deformation in the solid parts of the system although one could like to investigate an effects of thermoelasticity in the crystal and the surrounding ampoule. We will solve a flow of air in the furnace to account for a heat transfer by a convection therein. More importantly we shall solve a flow in the melt. Since phase interface ought to be driven by energy balance in a diffuse-interface manner we need to handle mechanics – i.e. linear momentum balance – also in this way. We simply adopt the way used many times (see [26, 42, 39, 40]) which penalizing velocity in solid phase by Darcy-type forcing. Together with consideration of Newtonian response (with no bulk viscosity) we have balance of linear momentum

$$\rho\dot{\mathbf{u}} = -\nabla p + \text{div}(\mu(\nabla\mathbf{u} + \nabla\mathbf{u}^\top)) - S\mathbf{u} + \rho\mathbf{g} \quad (2.22)$$

where  $\mu$  is dynamic viscosity of fluid,  $\mathbf{g}$  is gravity acceleration due to Earth and  $S$  is penalty function taking high value in solid phase and being zero in liquid

---

that very high purity of used substance enables substantial under-cooling when suddenly pulling the crystal out of the furnace by a significant displacement. This could be in principle predicted by phase-field model incorporating surface free energy and kinetic equation for phase-field or sharp-boundary model with kinetic interfacial condition like the Gibbs-Thomson equation (see Beckermann et al. [5, equation (23)] for treatment on a connection between these two approaches or Baldoni and Rajagopal [4, inequality (5.9)] giving far generalization of such condition).

phase. In the terms of Darcy's law  $S$  is related to permeability of porous media  $K$  through  $S = \mu/K$ . Usual form used for  $S$  is

$$S(\phi) = C \frac{(1 - \phi)^2}{\phi^3} \quad (2.23)$$

where  $\phi$  is porosity and  $C$  large constant. This equation is motivated by Kozeny-Carman formula (see [24]) which predicts a discharge of a stationary laminar flow through homogeneous porous media by considering the Poiseuille flow through a collection of straight ducts and rather heuristically accounting for geometry of pores. There is no clear connection between assumptions behind this formula and physics of the diffuse interface. One could rather consider equation (2.23) as a numerical penalty enforcing no flow in a solid phase.

As we did not specify in any way what measurable quantity is represented by phase-field  $c$  in preceding subsection we are free now to choose  $c = \phi$ . Considering density (2.18), viscosity  $\mu = \mu(\theta)^5$  and defining  $S(\theta) = S(c(\theta))$  we arrive at balance of linear momentum

$$\rho(\theta)\dot{\mathbf{u}} = -\nabla p + \operatorname{div}(\mu(\theta)(\nabla \mathbf{u} + \nabla \mathbf{u}^\top)) - S(\theta)\mathbf{u} + \rho(\theta)\mathbf{g} \quad (2.24)$$

As said above we understand mentioned Darcy-forcing-model as a mathematical penalization rather than a proper model of interface mechanics. Besides it misses surface tension, it does not model anything but rigid solid. In addition it penalizes movement against coordinate frame not against solid phase hence it could not be useful for describing homogeneous nucleation.

If we would like to take into account thermoelasticity of solid phase we could turn to some viscoelastic model (for example [32, 33]). We believe that this could be in principle coupled with phase-field so that models reduced to elastic and viscous behaviour in solid and liquid phase respectively. However it is not clear whether numerical implementation would be manageable.

As an interfacial condition for velocity on a surface between melt and protective atmosphere we choose continuity. It is obvious that normal velocity must be continuous and equal to surface velocity because of mass conservation on this surface. But condition for a tangential component could be relaxed to say Navier's slip condition, free-slip condition etc. We chose the continuity because anything else would require an additional major implementational and/or computational effort.

### 2.1.3 Mass balance

Mass balance will apply only to fluid regions and diffuse interface as we chose not to account for any deformation in solid parts of the system.

In accordance to previous subsections we will stick here to the case of equilibrium density  $\rho = \rho(\theta)$  but omit  $\theta$  argument for convenience.

It is well-known that the compressible Navier-Stokes equations (i.e. with full mass balance in the form (2.1)) supports sound waves. Numerical solution of

---

<sup>5</sup>We have no motivation to start with  $\mu = \mu(\theta, c)$  and interpreting viscosity of a solid phase hence we omit dependence of  $\mu$  on  $c$  whose inclusion could seem natural in view of preceding subsection.

such a problem with hyperbolic character requires special treatment. Regarding low Mach number flows one is usually not interested in these waves at all. The most prevalent way to suppress sound waves is using Boussinesq approximation. This consists in its simplest form of approximating mass balance (2.1) by

$$\operatorname{div} \mathbf{u} = 0 \quad (2.25)$$

and approximating density, capacity, conductivity etc. by constants

$$\rho = \bar{\rho}, \quad c_p = \bar{c}_p, \quad \dots$$

in all the terms of mass and energy balance (2.2),(2.3) except body force term  $\rho \mathbf{b} = \rho(\theta) \mathbf{g}$  which represents buoyancy and enables natural convection. In forced convection cases one calls this incompressible/isochoric approximation of flow rather than Boussinesq approximation.

Approximation (2.25) is not acceptable for us from two reasons. First one is that this is too crude unless

$$\rho(\theta_0) - \rho(\theta_1) \ll \rho(\bar{\theta}) \quad (2.26)$$

holds where  $\theta_0$ ,  $\theta_1$  and  $\bar{\theta}$  represents respectively the lowest, the highest and mean (in some sense) temperature of media in a flow process. This is not clearly the case at least for air in the furnace which flows up and down in the gap between furnace inner wall and the ampoule. Perturbative analysis of Boussinesq approximation and more precisely declared criteria for validity of the approximation were pronounced by Rajagopal, Ružička and Srinivasa [31].

But the second and the most important reason is related to the fact that the density of  $\text{PbCl}_2$  increases by not negligible amount during solidification. Densities of crystallic and liquid phase at melting point are  $5666 \text{ kg m}^{-3}$  and  $4951 \text{ kg m}^{-3}$  respectively (see Figure 2.2). Therefore domain  $\Omega$  (see Figure 2.1) must change its volume during solidification. Because  $\partial\Omega$  is material surface, melt surface  $\Sigma$  must move down while fraction of solid increases. It means that vertical component of the melt velocity  $u_z$  fulfills

$$u_z|_{\Sigma} = U < 0 \quad (2.27)$$

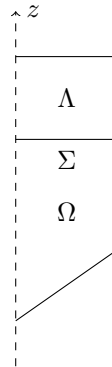


Figure 2.1: Domains representing interior of the ampoule.  $\Omega$  represents  $\text{PbCl}_2$  - either crystal and melt,  $\Lambda$  protective atmosphere and  $\Sigma = \partial\Omega \cap \partial\Lambda$  planar surface of the melt.



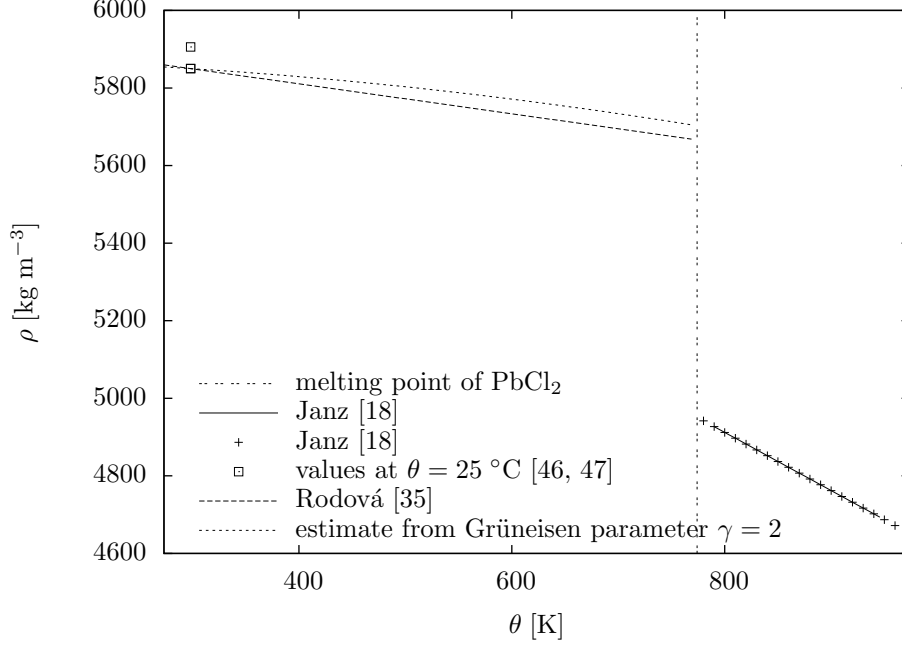


Figure 2.2: Density of  $\text{PbCl}_2$ . Experimental values and the estimate based on known value at 25 °C and assuming value of Grüneisen parameter - see [45].

with  $U$  independent of spatial coordinates while solidification takes place. This would be in contradiction with (2.25) or even so-called anelastic approximation

$$\operatorname{div} \rho \mathbf{u} = 0 \quad (2.28)$$

used usually in geosciences to describe low Mach number flows of such a depth that they do not meet (2.26). We therefore step into pseudo-incompressibility approximation of the form

$$\operatorname{div} \rho \mathbf{u} = \alpha_\Omega \quad \text{in } \Omega, \quad (2.29)$$

$$\operatorname{div} \rho \mathbf{u} = \alpha_\Lambda \quad \text{in } \Lambda \quad (2.30)$$

with  $\alpha_\Omega$ ,  $\alpha_\Lambda$  being spatially constant. Integrating (2.29),(2.30) over  $\Omega$ , using divergence theorem and (2.27) one gets

$$U \int_{\Sigma} \rho|_{\Omega} \, dS = \alpha_\Omega |\Omega|, \quad (2.31)$$

$$-U \int_{\Sigma} \rho|_{\Lambda} \, dS = \alpha_\Lambda |\Lambda| \quad (2.32)$$

Equations (2.29),(2.30) represents pseudo-incompressibility constraint and equations (2.27),(2.31) give interfacial condition for velocity which reads

$$u_z|_{\Sigma} = \frac{\alpha_\Omega |\Omega|}{\int_{\Sigma} \rho|_{\Omega} \, dS}, \quad (2.33)$$

$$u_z|_{\Sigma} = -\frac{\alpha_\Lambda |\Lambda|}{\int_{\Sigma} \rho|_{\Lambda} \, dS}. \quad (2.34)$$

To close the equations we need to provide equations for  $\alpha_\Omega$  and  $\alpha_\Lambda$ . Comparing (2.29),(2.30) with proper mass balance (2.1) one gets

$$\alpha_\Omega = -\frac{1}{|\Omega|} \int_\Omega \rho' dV, \quad (2.35)$$

$$\alpha_\Lambda = -\frac{1}{|\Lambda|} \int_\Lambda \rho' dV. \quad (2.36)$$

This ensures that mass is conserved in  $\Omega$  and  $\Lambda$  separately. We note that this approximation when discretized cannot be consistent with original mass balance (2.1) as  $\alpha_\Omega, \alpha_\Lambda$  are zero-order in space approximations to time-derivative  $-\rho'$  except special cases.

We pick the equation (2.33) rather than (2.34) for expressing interfacial velocity condition because isobaric expansion of solid and melt in  $\Omega$  is what steers surface movement and volume of gas in  $\Lambda$  not vice versa. This is basically caused by orders of magnitude difference in compressibilities of gas and condensed phases.

#### 2.1.4 Complete model

Let us have four time-dependent domains  $\bar{\Omega} \cup \bar{\Lambda}, \Delta, \Phi, \Psi$  whose movement is a priori known (see Figure 2.3; for real dimensions see Figure 1.3). Note that position of horizontal planar surface  $\Sigma = \partial\Omega \cap \partial\Lambda$  is not a priori known and is a consequence of mass conservation in  $\Omega$ . Values of all material coefficients are in table 2.1. Then the problem is to find the unknowns  $\Sigma, \mathbf{u}, p, \theta, \alpha$  such that

- $\Sigma = \partial\Omega \cap \partial\Lambda$  is horizontal and planar time-dependent domain,
- $\mathbf{u}$  and  $p$  are functions of time and coordinates continuous in the each of their domain  $\Omega, \Lambda, \Delta$ ,
- $\theta$  is continuous function of time and coordinates in the domain  $\bar{\Omega} \cup \bar{\Lambda} \cup \bar{\Delta} \cup \bar{\Phi} \cup \bar{\Psi}$ ,
- $\alpha$  is function of time and coordinates defined in  $\Omega$  and  $\Lambda$  which is spatially constant in each of its domain separately,
- mass and momentum balance

$$\text{div}(\rho \mathbf{u}) = \alpha, \quad (2.37)$$

$$\rho \dot{\mathbf{u}} = -\nabla p + \text{div}(\mu(\nabla \mathbf{u} + \nabla \mathbf{u}^\top)) - S\mathbf{u} + \rho \mathbf{g}, \quad (2.38)$$

$$\alpha = \begin{cases} -\frac{1}{|\Omega|} \int_\Omega \rho' dV & \text{in } \Omega \\ -\frac{1}{|\Lambda|} \int_\Lambda \rho' dV & \text{in } \Lambda \\ 0 & \text{in } \Delta \end{cases}, \quad (2.39)$$

are fulfilled in  $\Omega, \Lambda$  and  $\Delta$ ,

- energy balance

$$\rho c_p^{\text{eff}} \dot{\theta} = \text{div}(\kappa \nabla \theta), \quad (2.40)$$

is fulfilled in  $\Omega, \Lambda, \Delta, \Phi$  and  $\Psi$ ,

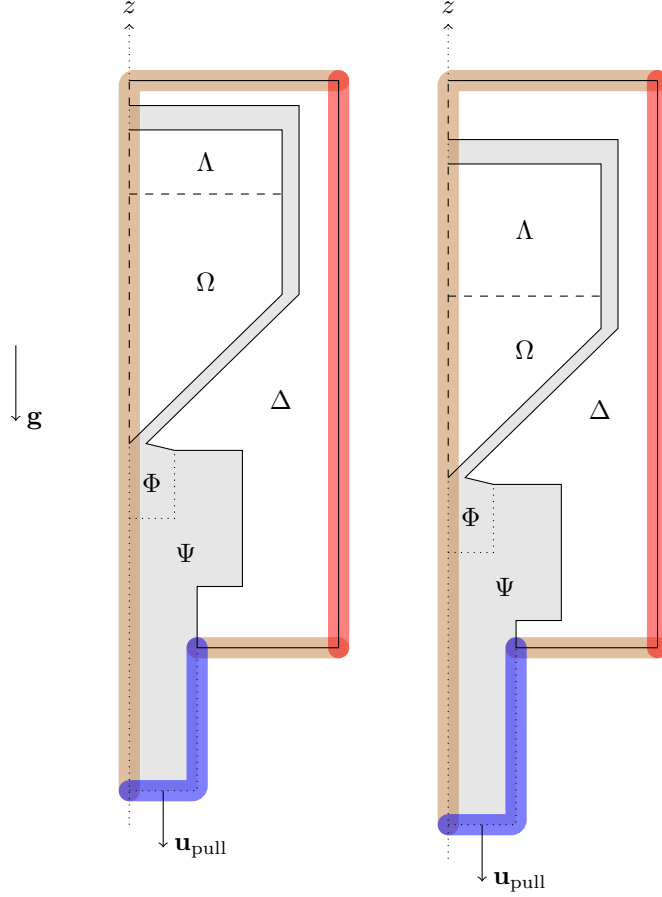


Figure 2.3: Schematic layout of computational domains:  $\Omega$  – crystal and melt,  $\Lambda$  – protective atmosphere,  $\Delta$  – air in furnace,  $\Phi$  – ampoule,  $\Psi$  – holder; velocity boundary conditions: — no-slip, ---- free-slip, ..... not applicable; temperature boundary conditions: ■ Dirichlet cooling  $\theta = 350$  K, ■ Dirichlet heating - see Figure 1.3, ■ thermal insulation (zero Neumann condition). Note that domains  $\bar{\Omega} \cup \bar{\Lambda}$ ,  $\Phi$  and  $\Psi$  are rigid and they are moving downwards with constant velocity  $\mathbf{u}_{\text{pull}}$  so that  $\Delta$  is being deformed such that  $\partial\Delta \setminus (\bar{\Phi} \cup \bar{\Psi})$  stays at rest.

- $\mathbf{u}$  is continuous on  $\Sigma$ <sup>6</sup>,
- velocity  $\mathbf{u}$  which is being a velocity of  $\Sigma$  as well fulfills

$$u_z|_{\Sigma} = -\frac{\alpha|_{\Omega}|\Omega|}{\int_{\Sigma} \rho|_{\Omega} dS} \quad (2.41)$$

due to mass conservation in  $\Omega$ ,

- no tangential force acts on  $\Sigma$ , i.e.

$$\tau \cdot (\mathbf{T}|_{\Omega} - \mathbf{T}|_{\Lambda}) \mathbf{n} = 0 \quad \text{on } \Sigma \quad (2.42)$$

for all  $\mathbf{n}$ ,  $\tau$  unit normal and tangential vectors of the surface  $\Sigma$  respectively, where  $\mathbf{T} = -p\mathbf{I} + \mu(\nabla\mathbf{u} + \nabla\mathbf{u}^{\top})$ ,

<sup>6</sup>We choose this interfacial condition merely for an implementational ease involved.

- free-slip condition holds on symmetry axis, i.e.

$$\left. \begin{array}{l} \mathbf{u} \cdot \mathbf{n} = 0 \\ \tau \cdot \mathbf{Tn} = 0 \end{array} \right\} \quad \text{on } \{r = 0\} \cap (\overline{\Omega} \cup \overline{\Sigma} \cup \overline{\Delta}), \quad (2.43)$$

for all  $\mathbf{n}$ ,  $\tau$  unit normal and tangential vectors of the axis  $\{r = 0\}$  respectively, where  $\mathbf{T}$  is given as above,

- no-slip condition (given by movement of the respective boundaries) for  $\mathbf{u}$  holds on other velocity boundaries,
- heat flux  $-\kappa \nabla \theta$  is continuous on every interior interface and is zero on insulation boundaries given in Figure 2.3,
- temperature Dirichlet condition for  $\theta$  given in Figure 2.3 is being acquired,
- initial conditions for  $\mathbf{u}$ ,  $p$ ,  $\theta$  and  $\alpha$  are attained in respective domains.

We note again that we choose continuity of tangential component of  $\mathbf{u}$  on  $\Sigma$  just because of computational ease.

We must remark that if one forgets all the boundary conditions given on  $\{r = 0\}$  and imagines that all the domains are toroidal so that just their half-section is showed in Figure 2.3, one can regard this as 3D formulation involving no assumption on a symmetry of a solution. Role of these boundary conditions will be exposed in following sections.

One can take an advantage of the fact that pulling velocity  $\mathbf{u}_{\text{pull}}$  is constant hence a frame of reference connected with the ampoule is inertial as well. Thus in domains  $\Omega$  and  $\Lambda$  we can solve for velocity relative to the ampoule whereas in domain  $\Delta$  we can take laboratory velocity, without any modification to the equations except values of the Dirichlet conditions.

Now we must mention that problem as given above has not good mathematical meaning. Attentive reader could indeed object that we did not specified sufficient differentiability the unknowns should have in order to field equations had a good meaning. We were sloppy here because the data does not allow for classical formulation anyway. One can observe that at least velocity boundary/interfacial conditions as specified possesses discontinuity in points where moving and still boundaries/interfaces meet. Remedy to this is a weak formulation of the problem which will be treated in next sections.

## 2.2 Weak form of equations

At first consider open domains  $\widehat{\Omega}$ ,  $\widehat{\Lambda}$ ,  $\widehat{\Delta}$ ,  $\widehat{\Phi}$ ,  $\widehat{\Psi}$  and  $\widehat{\Sigma} = (\partial\widehat{\Omega} \cap \partial\widehat{\Lambda})^\circ$  as three-dimensional and rotationally symmetric so that respective domains in Figure 2.3 represent the half-section. Next we define  $\widehat{V}$  as a subset of Sobolev space  $H^1(\widehat{\Omega} \cup \widehat{\Sigma} \cup \widehat{\Lambda} \cup \widehat{\Delta})^3$  with zero trace of a respective component on the velocity Dirichlet boundaries defined above,<sup>7</sup> Lebesgue space  $\widehat{P} = L^2(\widehat{\Omega} \cup \widehat{\Lambda} \cup \widehat{\Delta})$ <sup>8</sup> and  $\widehat{Q}$  as a subset of  $H^1(\widehat{\Omega} \cup \widehat{\Lambda} \cup \widehat{\Delta} \cup \widehat{\Phi} \cup \widehat{\Psi})$  with zero trace on temperature Dirichlet boundaries.

<sup>7</sup>Note that  $\widehat{V}$  is constrained to zero trace also on internal interface  $\widehat{\Sigma}$ .

<sup>8</sup>Note that  $\widehat{P}$  admits discontinuity (of traces) on  $\widehat{\Sigma}$  in comparison with  $\widehat{V}$ .

$\Omega$	$\rho = \rho^S + (\rho^L - \rho^S)H^0\left(\frac{\theta - \theta_m}{\epsilon}\right)$ $\rho^L = 6112 - 1.5 \theta$ $\rho^S = 5965.1 - 0.3861 \theta$ $c_p^{\text{eff}} = c_p^S + (c_p^L - c_p^S)H^0\left(\frac{\theta - \theta_m}{\epsilon}\right) + L/\epsilon \delta^1\left(\frac{\theta - \theta_m}{\epsilon}\right)$ $c_p^S = 0.02903/M \theta + 68.45/M$ $c_p^L = 11.504/M$ $L = 21883/M, \quad M = 0.2781, \quad \theta_m = 774$ $\kappa = 7.132 \times 10^{-7} \theta^2 + 0.0001932 \theta$ $\mu = 4.5356 \times 10^{-3}$	 [18] [35]  [9] [9] [9]  [18]
$\Lambda$	$\rho = 0.4572 - 5.714 \times 10^{-4}(\theta - \theta_m)$ $c_p = 30/0.0365$ $\kappa = 0.04$ $\mu = 3.66 \times 10^{-5}$	IGL [27] [27] [27]
$\Delta$	$\rho = 0.46 - 6 \times 10^{-4}(\theta - \theta_m)$ $c_p = 1000$ $\kappa = 0.05$ $\mu = 3.625 \times 10^{-5}$	IGL
$\Phi$	$\rho = 2203$ $c_p = 45.3/0.06$ $\kappa = 1.3$	[44] [44] [44]
$\Psi$	$\rho = 8908$ $c_p = 26.07/0.0587$ $\kappa = 90.9$	Fe Fe Fe
$H^0(x) = \begin{cases} 0 & x \leq -1 \\ (x+1)/2 & -1 < x < 1 \\ 1 & x \geq 1 \end{cases}$ $\delta^1(x) = \begin{cases} (x+1)^2(x-1^2) & -1 < x < 1 \\ 0 & x \leq -1 \text{ or } x \geq 1 \end{cases}$		

Table 2.1: Used values of material coefficients.  $M$  is molar mass of  $\text{PbCl}_2$ ,  $H^0$  is  $\mathcal{C}^0$ -approximation to Heaviside function and  $\delta^1$  is  $\mathcal{C}^1$ -approximation to Dirac- $\delta$  distribution. Fe means *value of iron taken instead* and IGL is *ideal gas law*.

Finally consider  $\mathbf{u}^D \in H^1(\widehat{\Omega} \cup \widehat{\Sigma} \cup \widehat{\Lambda} \cup \widehat{\Delta})^3$  and  $\theta^D \in H^1(\widehat{\Omega} \cup \widehat{\Lambda} \cup \widehat{\Delta} \cup \widehat{\Phi} \cup \widehat{\Psi})$  being some representatives of these Dirichlet conditions.

The task is then to find  $\mathbf{u}$ ,  $p$ ,  $\theta$ ,  $\alpha$  and  $\widehat{\Sigma}$  such that

$$\mathbf{u}(t) - \mathbf{u}^D(t) \in \widehat{V}, \quad \mathbf{u}'(t) \in L^2(\widehat{\Omega} \cup \widehat{\Lambda} \cup \widehat{\Delta}), \quad (2.44)$$

$$p(t) \in \widehat{P}, \quad (2.45)$$

$$\theta(t) - \theta_D(t) \in \widehat{Q}, \quad \theta'(t) \in L^2(\widehat{\Omega} \cup \widehat{\Lambda} \cup \widehat{\Delta} \cup \widehat{\Phi} \cup \widehat{\Psi}), \quad (2.46)$$

$$0 = \int_{\widehat{\Omega} \cup \widehat{\Lambda} \cup \widehat{\Delta}} q [\operatorname{div}(\rho \mathbf{u}) - \alpha] \, dV \quad \forall q \in \widehat{P}, \quad (2.47)$$

$$\alpha = \begin{cases} -\frac{1}{|\widehat{\Omega}|} \int_{\widehat{\Omega}} \rho' \, dV & \text{in } \widehat{\Omega} \\ -\frac{1}{|\widehat{\Lambda}|} \int_{\widehat{\Lambda}} \rho' \, dV & \text{in } \widehat{\Lambda} \\ 0 & \text{in } \widehat{\Delta} \end{cases}, \quad (2.48)$$

$$0 = \int_{\widehat{\Omega} \cup \widehat{\Lambda} \cup \widehat{\Delta}} [\rho(\mathbf{u}' + \nabla \mathbf{u} \mathbf{u}) \cdot \mathbf{v} - p \operatorname{div} \mathbf{v} + \mu(\nabla \mathbf{u} + \nabla \mathbf{u}^\top) \cdot \nabla \mathbf{v} - \rho \mathbf{g} \cdot \mathbf{v} + S \mathbf{u} \cdot \mathbf{v}] \, dV \quad \forall \mathbf{v} \in \widehat{V}, \quad (2.49)$$

$$0 = \int_{\widehat{\Omega} \cup \widehat{\Lambda} \cup \widehat{\Delta} \cup \widehat{\Phi} \cup \widehat{\Psi}} [\rho c_p^{\text{eff}}(\theta' + \mathbf{u} \cdot \nabla \theta) \eta + \kappa \nabla \theta \cdot \nabla \eta] \, dV \quad \forall \eta \in \widehat{Q} \quad (2.50)$$

holds almost everywhere in time interval  $(0, T)$  and some initial conditions for the quantities  $\mathbf{u}$ ,  $\theta$  and  $\Sigma$  are being attained in  $t = 0$ . We note that we are slightly sloppy treating time-dependence of the problem. Proper way would be to employ the theory of Bochner spaces, polish a sense of time derivatives and initial condition. We relieve us from doing this by assuming sufficient time-regularity.

All the coefficients except  $S$  are  $L^\infty$  functions in their respective domains because these are continuous functions of  $\theta$  which is essentially bounded due to maximum principle applying to heat equation (2.50).<sup>9</sup> Coefficient  $S = S(c(\theta))$  given by (2.23) takes infinite values in the solid phase where  $c = 0$ . Hence (2.23) must be modified somehow so that  $S \in L^\infty(\Omega)$ . For now we just assume this holds.

Once all the coefficients are essentially bounded we see that chosen trial and test spaces render all the terms in (2.47)–(2.50) finite (convective terms are rescued by the Sobolev embedding).

This weak formulation is non-standard in the involvement of the pseudo-incompressibility condition (2.47) rather than standard  $0 = \int q \operatorname{div} \mathbf{u} \, dV$  constraint. Also note that integral in (2.47) is computed separately on domains  $\widehat{\Omega}$  and  $\widehat{\Lambda}$  to avoid integration of Dirac  $\delta$  due to discontinuity of  $\rho$  across interface  $\widehat{\Sigma}$ .

---

<sup>9</sup>We don't know how to proof the maximum principle. Nevertheless we would like to expect holding it.

## 2.3 Cylindrical coordinates

Now we will proceed with transition to cylindrical coordinates  $r, \varphi, z$  given by

$$x = r \cos \varphi, \quad (2.51)$$

$$y = r \sin \varphi, \quad (2.52)$$

$$z = z \quad (2.53)$$

in order that we can exploit the symmetry of the problem. Hence we first assume that no quantity in (2.47)–(2.50) depends on angle  $\varphi$  and also assume that velocity field has no swirl, i.e.  $\mathbf{u} = u_r \hat{\mathbf{r}} + u_z \hat{\mathbf{z}}$  where  $\hat{\mathbf{r}}, \hat{\boldsymbol{\varphi}}, \hat{\mathbf{z}}$  is unit basis induced by cylindrical coordinates. Then the following relations hold

$$dV = 2\pi r dr dz, \quad (2.54)$$

$$dS = 2\pi r dr \quad \text{for horizontal } dS, \quad (2.55)$$

$$\begin{aligned} \operatorname{div} \mathbf{y} &= y_{r,r} + y_{z,z} + y_r/r \quad \forall \mathbf{y} \text{ axi-symmetric, differentiable,} \\ &\quad \text{no-swirl vector,} \end{aligned} \quad (2.56)$$

$$\mathbf{x} \cdot \mathbf{y} = x_r y_r + x_z y_z \quad \forall \mathbf{x}, \mathbf{y} \text{ axi-symmetric, no-swirl vectors}^{10}, \quad (2.57)$$

$$\nabla \mathbf{u} \mathbf{u} = (u_{r,r} u_r + u_{r,z} u_z) \hat{\mathbf{r}} + (u_{z,r} u_r + u_{z,z} u_z) \hat{\mathbf{z}}, \quad (2.58)$$

$$\begin{aligned} (\nabla \mathbf{u} + \nabla \mathbf{u}^\top) \cdot \nabla \mathbf{v} &= u_{r,r} v_{r,r} + (u_{r,z} + u_{z,r})(v_{r,z} + v_{z,r})/4 \\ &\quad + u_{z,z} v_{z,z} + u_r v_r / r^2. \end{aligned} \quad (2.59)$$

One can now become interested what are suitable function spaces for  $u_r, u_z, p, \theta$ . Deparis [11][Proposition 1.2.1] shows that particular weighted Sobolev spaces are isomorphic to no-swirl, axi-symmetric subsets of spaces  $\widehat{V}, \widehat{P}$  and  $\widehat{Q}$  and summarizes or proves many technical results regarding analysis of Stokes and Navier-Stokes problem and their particular finite-element approximations.

To be specific, let space  $L_\alpha^p(D)$  is defined as the set of measurable functions with finite norm

$$\|w\|_{L_\alpha^p(D)} = \left( \int_D |w|^{p\alpha} dr dz \right)^{1/p}. \quad (2.60)$$

Next let  $H_1^1(D) \subset L_1^2(D)$  such that norm

$$\|w\|_{H_1^1(D)} = \left( \|w\|_{L_1^2(D)}^2 + \|w_{r,r}\|_{L_1^2(D)}^2 + \|w_{z,z}\|_{L_1^2(D)}^2 \right)^{1/2} \quad (2.61)$$

is finite. Finally let us define  $V_1^1(D) = H_1^1(D) \cap L_{-1}^2(D)$  equipped with norm

$$\|w\|_{V_1^1(D)} = \left( \|w\|_{L_{-1}^2(D)}^2 + \|w_{r,r}\|_{L_1^2(D)}^2 + \|w_{z,z}\|_{L_1^2(D)}^2 \right)^{1/2}. \quad (2.62)$$

It can be shown that functions in  $V_1^1(D)$  have zero trace on axis  $r = 0$ .

Let domains  $\Omega, \Lambda, \Delta, \Phi, \Psi$  and  $\Sigma = (\partial\Omega \cap \partial\Lambda)^\circ$  are half-sections of corresponding hatted domains as shown in Figure 2.3. Now we can define spaces  $V_r$  and  $V_z$  for radial velocity  $u_r$  and axial velocity  $u_z$  as a subsets of  $V_1^1(\Omega \cup \Sigma \cup \Lambda \cup \Delta)$

<sup>10</sup>This relation holds also for gradients of axi-symmetric scalars in place of vectors.

and  $H_1^1(\Omega \cup \Sigma \cup \Lambda \cup \Delta)$  respectively subject to appropriate zero Dirichlet constraints. Pressure space is simply  $P = L_1^2(\Omega \cup \Lambda \cup \Delta)$  and temperature space  $Q$  is a subset of  $H_1^1(\overline{\Omega \cup \Lambda \cup \Delta \cup \Phi \cup \Psi})$  subject to zero temperature conditions given above.

Assuming axial symmetry and no-swirl we can now reformulate our problem (2.44)–(2.50) using transformations (2.54)–(2.59). Then task is to find  $u_r$ ,  $u_z$ ,  $p$ ,  $\theta$ ,  $\alpha$  and  $\widehat{\Sigma}$  such that

$$u_r(t) - u_r^D(t) \in V_r, \quad u'_r(t) \in L_1^2(\Omega \cup \Lambda \cup \Delta), \quad (2.63)$$

$$u_z(t) - u_z^D(t) \in V_z, \quad u'_z(t) \in L_1^2(\Omega \cup \Lambda \cup \Delta), \quad (2.64)$$

$$p(t) \in P, \quad (2.65)$$

$$\theta(t) - \theta^D(t) \in Q, \quad \theta'(t) \in L_1^2(\Omega \cup \Lambda \cup \Delta \cup \Phi \cup \Psi), \quad (2.66)$$

$$0 = \int_{\Omega \cup \Lambda \cup \Delta} q [(\rho u_r)_{,r} + (\rho u_z)_{,z} + \rho u_r/r - \alpha] 2\pi r dr dz \quad \forall q \in P, \quad (2.67)$$

$$\alpha = \begin{cases} -\frac{1}{|\Omega|} \int_{\Omega} \rho' 2\pi r dr dz & \text{in } \Omega \\ -\frac{1}{|\Lambda|} \int_{\Lambda} \rho' 2\pi r dr dz & \text{in } \Lambda \\ 0 & \text{in } \Delta \end{cases}, \quad (2.68)$$

$$0 = \int_{\Omega \cup \Lambda \cup \Delta} [\rho (u'_r + u_{r,r} u_r + u_{r,z} u_z) v_r + \rho (u'_z + u_{z,r} u_r + u_{z,z} u_z) v_z$$

$$+ \mu (u_{r,r} v_{r,r} + (u_{r,z} + u_{z,r})(v_{r,z} + v_{z,r})/4 + u_{z,z} v_{z,z} + u_r v_r/r^2)$$

$$- p (v_{r,r} + v_{z,z} + u_r/r) - \rho g_z v_z + S(u_r v_r + u_z v_z)] 2\pi r dr dz \quad \forall \mathbf{v} \in V_r \times V_z,$$

$$(2.69)$$

$$0 = \int_{\overline{\Omega \cup \Lambda \cup \Delta \cup \Phi \cup \Psi}} [\rho c_p^{\text{eff}} (\theta' + \theta_{,r} u_r + \theta_{,z} u_z) \eta + \kappa (\theta_{,r} \eta_{,r} + \theta_{,z} \eta_{,z})] 2\pi r dr dz \quad \forall \eta \in Q \quad (2.70)$$

Note that  $1/r$  term in (2.67) and in the pressure term of (2.69) is canceled by Jacobian of volume element  $r$ . But there remains term  $2\pi \int \mu u_r v_r / r dr dz$  having  $1/r$  factor. This is clearly integrable thanks to a choice of  $V_r$  function space.

We must mention that spaces  $V_r$ ,  $V_z$  and  $P$  depend on the position of interface  $\Sigma$  which is driven by (2.41) which we did not include explicitly to the problem formulation. Also value  $u_z^D$  is given by the same equation. Technically this makes all these “quantities” unknowns. We are not sure whether the problem is still well-posed under these conditions. There is also an option reformulating Dirichlet constraints on  $\Sigma$  using Lagrange multipliers. We leave it in this state with note that numerical procedure we will present in next chapter treats this coupling successfully in very simple explicit way and the continuous formulation was rather reverse-engineered from the numerical procedure.



## 2.4 Notes on Allen-Cahn type model

Allen-Cahn equation<sup>11</sup>

$$\rho \dot{c} = \gamma \left( \frac{3}{2} \frac{\sigma \epsilon}{\rho} \Delta c - 12 \frac{\sigma}{\epsilon} (c+1)c(c-1) \right) \quad (2.71)$$

originating in work [2] is evolution equation for phase-field  $c$  subject to species conversion driven by particular potentials which will be given hereafter. The equation can also be derived from variational formulation. In this section interface width  $\epsilon$  has dimension of length instead of temperature. Constant  $\sigma$  is surface tension and  $\gamma$  is kinetic coefficient required to be positive by the 2nd law of thermodynamics.

Equation (2.71) (or similar Allen-Cahn-like equations) can be coupled to thermomechanical framework in different ways. In subsection 2.4.2 we will treat on one particular given in [15]. We recommend a reader to read this work before stepping into subsection 2.4.2 because there is not enough room to rephrase this work here.

But first we shortly take a look on surface tension from a perspective of classical thermodynamics.

### 2.4.1 Classical thermodynamics of interface

Classical thermodynamics of interface might be described by fundamental relation

$$dU^I = \theta dS^I + \sigma dA^I \quad (2.72)$$

where  $U^I$  is internal energy of interface,  $S^I$  entropy of interface,  $A^I$  surface area of interface and  $\sigma$  is so called surface tension or surface energy.

Now we present an argument by Ondřej Souček showing that surface tension  $\sigma$  can be interpreted as a surface density of Helmholtz potential:

Consider fundamental equation of an interface (2.72). Also assume that internal energy  $U^I(S^I, A^I)$  is a function homogeneous of order one, i.e.

$$U^I(\lambda S^I, \lambda A^I) = \lambda U^I(S^I, A^I) \quad \forall \lambda > 0. \quad (2.73)$$

Then one can use classical Euler's argument to obtain Euler equation. Differentiating (2.73) w.r.t.  $\lambda$  and using (2.72) we obtain

$$U^I = \theta S^I + \sigma A^I. \quad (2.74)$$

Dividing by  $A^I$  one gets

$$\sigma = \frac{U^I}{A^I} - \theta \frac{S^I}{A^I} \quad (2.75)$$

hence one can say that  $\sigma$  is surface density of Helmholtz potential.

(Ondřej Souček, June 10, 2013, personal correspondence)

---

<sup>11</sup>Form with the unusual scaling is presented. This is consistent with functionals given hereafter.

### 2.4.2 Diffuse interface thermodynamics

Let us split Helmholtz free energy density into bulk part  $f^B$  and interfacial part  $f_\epsilon^I$  and assume special dependence on quantities  $\theta, \nu, c, \nabla c$

$$f(\theta, \nu, c, \nabla c) = f^B(\theta, \nu, c) + f_\epsilon^I(\nu, c, \nabla c). \quad (2.76)$$

First term is motivated by the set-up of subsection 2.1.1 with the exception that now we start with Helmholtz potential. For a second term we take

$$f_\epsilon^I(\nu, c, \nabla c) = \nu \left[ 12 \frac{\sigma}{\epsilon} c^2 (1-c)^2 + \frac{3}{4} \sigma \epsilon |\nabla c|^2 \right] \quad (2.77)$$

with constant  $\sigma$ . This formula is motivated by classical functional for free energy

$$F[c] = \int [f(c) + \sigma/2 |\nabla c|^2] \, dV \quad (2.78)$$

introduced in original Allen-Cahn and Cahn-Hilliard models [2, 8]. In particular we use the form similar to [6][equation (1)]. In this work there is shown that in one dimension functional  $c \mapsto \int \rho f_\epsilon^I \, dx$  takes minimal value  $\sigma$  under the species-conserving constraint  $\int c \, dx = \text{const}$ . This demonstrates connection with sharp interface energy

$$\int \sigma \, dS \quad (2.79)$$

used in classical thermodynamics. Particularly interesting is the fact that minimal value does not depend on the value of  $\epsilon$ .

Very promising way of how to incorporate classical diffuse interface models by Allen, Cahn and Hilliard into continuum thermo-mechanical framework was proposed recently by Heida, Málek and Rajagopal in [16, 15]. We are especially interested in the latter work which applies to a system subject to species conversion. In this work surface free energy (2.78) is taken and very special internal energy of the system is considered. The simplest possible non-trivial entropy production is assumed and constitutive relations for fluid-like multi-phase system are then derived using Ziegler's principle of maximal entropy production (see [23]) although there is some freedom in the choice of entropy flux during this procedure.

A knowledge of a concrete function dependency (2.76) gives us full equilibrium information about the system considered. Now we proceed by exploiting consequences of this dependency as we think that otherwise convincing diffuse interface model suggested in [15] utilizes a quite restrictive form of a thermodynamic potential. In particular there is chosen internal energy of the form

$$e(\eta, \nu, c, \nabla c) = e_0(\eta, \nu) + f(c) + \nu \sigma/2 |\nabla c|^2. \quad (2.80)$$

Performing partial Legendre transform (see [41][section 10.1]) in variables  $\eta, \nu$  (up to the sign) one gets Gibbs potential

$$g(\theta, p, c, \nabla c) = g_0(\theta, p, \nabla c) + f(c) + \nu_0(\theta, p, \nabla c) \sigma/2 |\nabla c|^2. \quad (2.81)$$

with  $g_0$  and  $\nu_0$  being in a particular relation with  $e_0$  but this is not important. Difference  $g(\theta, p, 1, \nabla c) - g(\theta, p, 0, \nabla c) = f(1) - f(0)$  is constant hence the same

phase is always preferred regardless of temperature and pressure (or no phase at all when the difference is zero). This is very restrictive property disallowing a description of macroscopic phase-transitions.

We now show that potential (2.76) is a remedy to this problem. We will again incorporate enthalpy formulation of energy balance (2.6). We first calculate pressure

$$p = - \left( \frac{\partial f}{\partial \nu} \right)_{\theta, c, \nabla c} = p^B(\theta, \nu, c) + p_\epsilon^I(c, \nabla c) \quad (2.82)$$

where bulk part of pressure is given by

$$p^B(\theta, \nu, c) = - \frac{\partial f^B(\theta, \nu, c)}{\partial \nu} \quad (2.83)$$

and interfacial pressure is given by

$$p_\epsilon^I(c, \nabla c) = - \frac{\partial f_\epsilon^I(\nu, c, \nabla c)}{\partial \nu} = - \frac{f_\epsilon^I}{\nu} = - \left[ 12 \frac{\sigma}{\epsilon} c^2 (1-c)^2 + \frac{3}{4} \sigma \epsilon |\nabla c|^2 \right] \quad (2.84)$$

which is negative so that interface is coherent.

Now we assume that (2.83) is invertible in  $\nu$  so we can write

$$\nu = \hat{\nu}(\theta, p^B, c). \quad (2.85)$$

We also calculate entropy

$$\eta = - \left( \frac{\partial f}{\partial \theta} \right)_{\nu, c, \nabla c} = \eta^B(\theta, \nu, c) + \eta_\epsilon^I \quad (2.86)$$

where bulk entropy is

$$\eta^B(\theta, \nu, c) = - \frac{\partial f^B(\theta, \nu, c)}{\partial \theta} \quad (2.87)$$

and interfacial entropy  $\eta_\epsilon^I$  is zero. Relaxing constant  $\sigma$  to  $\sigma = \sigma(\theta)$  in (2.77) would induce non-trivial interfacial entropy  $\eta_\epsilon^I = \eta_\epsilon^I(\theta, \nu, c, \nabla c)$ . This would prevent us from deriving particularly simple energy balance hereinafter so we avoided it. But it can be easily considered.

Now we calculate enthalpy

$$\begin{aligned} h &= f + p\nu + \theta\eta \\ &= f^B(\theta, \hat{\nu}(\theta, p^B, c), c) + \underbrace{f_\epsilon^I + p_\epsilon^I \nu}_{=0 \text{ due to (2.84)}} + p^B \hat{\nu}(\theta, p^B, c) + \theta \eta^B(\theta, \hat{\nu}(\theta, p^B, c), c) \\ &=: h^B(\theta, p^B, c) \end{aligned} \quad (2.88)$$

We obtained a form of enthalpy which does not depend on  $\nabla c$ . Little drawback is that it depends on *bulk pressure*  $p^B$  instead of true pressure  $p$ . But this difference can be probably ignored if interface possesses small curvature so that (negative) interfacial pressure is small compared to bulk pressure which is to be mainly induced by large ambient pressure. This is somewhat analogical to the situation with slow flows under large ambient pressure constraint as described in subsection 2.1.1. If we neglect difference between  $p^B$  and  $p$  we obtained *exactly* (2.13).

If we would like to express enthalpy without the  $p \approx p^B$  approximation we could express density in (2.88) as  $\nu = \hat{\nu}(\theta, p - p_\epsilon^I(c, \nabla c), c)$  so we would not be able to rule-out  $\nabla c$  from energy balance.

By similar calculations we can compute also internal energy in its natural variables

$$e = e^B(\eta, \nu, c) + f_\epsilon^I(\nu, c, \nabla c). \quad (2.89)$$

We omit relation of  $e^B$  to known functions as it is not important here. It is crucial that (2.89) is a slight generalization of (2.80) so that all the constitutive relations derived in [15] are compatible and valid (under assumptions therein) with potential (2.76). Basically these relations count Newtonian fluid with added surface tension, Fourier law (possibly with added particle heat depending on chosen form of entropy flux) and Allen-Cahn type kinetic equation for phase-field  $c$  similar to (2.71).

Now we can turn back to our original problem of  $\text{PbCl}_2$  single crystal growth. The Allen-Cahn model [15], (2.76) would require some modification describe solid phase. The approach of subsection 2.1.2 would work but it is not apparent whether additional interfacial mechanics of Allen-Cahn model keeps sense when modified by such a heuristic, rather numerical workaround. One could also appreciate kinetic character of phase-field equation which could enable shifting actual melting temperature downwards with rapid growth rates. But still we have no idea what is the value of relevant kinetic coefficient as well as surface energy  $\sigma$  for crystal-melt interface of  $\text{PbCl}_2$ . Simply said Allen-Cahn model would bring us a little of new behaviour based on unknown material coefficient values at a cost of additional implementational and computational effort.

Interesting research topic regarding Allen-Cahn models could be finding a correspondence to models which relate surface tension with latent heat of vaporization (see [13]). This probably does not apply at all to solid-liquid phase transitions or it is at least not known.

### 3. Numerical algorithm

For a numerical implementation of the weak form of the model described in preceding chapter we have chosen FEniCS [21]. FEniCS Project is a free collection of libraries for automated solution of partial differential equations using finite element method. Automation here means that efficient low-level machine code for assembling element tensors is automatically generated by FFC (FEniCS form compiler) taking a form and a finite element specified by user as input. This code is independent of a particular mesh. During an actual computation a mesh is generated or imported and system tensors are assembled by iterating over mesh entities and invoking this code. Many efficient third-party libraries then can be used to solve for linear systems of algebraic equations. User's task is merely programming a solution algorithm in terms of coupling a discretization in time and space, a movement of a mesh, a linearization of a problem, etc. The most of these particular tasks is managed by high-level interface DOLFIN.

Not insignificant amount of work behind this thesis consists of bug-fixes and minor features being implemented into DOLFIN. As a result the code developed for solution of our problem runs with current development version of FEniCS. Specific revision of FEniCS components needed is specified in the enclosed source code.

We have tried to develop an algorithm which would work in parallel. Vast amount of FEniCS features works in parallel but there are few exception whose parallelization is under development or on plan. A major such exception is assembling of integrals over interior facets. Therefore we have a priori chosen to avoid these integrals. As a result we chose the possibly unrealistic interfacial condition for tangential velocity on  $\Sigma$  given above.

As we need to solve problem on moving domains, incorporated meshes will need to be deformed. In our case (and in the most cases in practice) maximal deformation of mesh is bounded by a requirement on its quality and on preservation of its topology<sup>1</sup>. As a result one needs from time to time to create a new mesh and project fields onto it. Such a projection produces substantial numerical error which must be attenuated by numerical scheme. Usual Crank-Nicolson scheme would require stringent restriction on time-step. We therefore choose backward Euler method for time discretization. One would prefer higher-order method but whole algorithm is such a complicated because of a moving mesh and unusual mass balance constraint that we would not reach at least a second order time-accuracy of a whole algorithm. Besides other things an involved growth process is slow, near-equilibrium hence accumulation effects are not of such an importance.

Developed code supports parallel execution using MPI (Message Passing Interface) but there are some practical consideration. First of all projections on non-matching meshes in parallel are not yet supported in FEniCS. We developed a hack requiring changes in DOLFIN source code which is not suitable for merging into main development branch. Actually it solves the issue in quite inefficient way.<sup>2</sup> As a second, we observed some problems during parallel computations on

---

<sup>1</sup>The latter demand prevents a situation when determinant of the deformation gradient is not strictly positive. Of course one would not call this by deformation in continuum-mechanical sense.

<sup>2</sup>Our solution – `serial-meshes` branch of DOLFIN is available at <https://bitbucket>.

the Karlín cluster<sup>3</sup>. We did not reliably discovered a cause but we suspect an outdated OpenMPI library although we cannot exclude a possible bug in our code, FEniCS or a stack of other used libraries.

### 3.1 Arbitrary Lagrangian–Eulerian formulation

As we noted in section 2.2 we did not treat time-dependence of the problem (2.44)–(2.50) precisely. Possible approach for giving a sense to term with time-derivative of some Sobolev function  $\phi$  consists of formally using equality

$$\int \phi' \psi \, dV = \frac{d}{dt} \int \phi \psi \, dV \quad (3.1)$$

where  $\psi$  is corresponding test function independent of time. Then one does not need to bother with Bochner spaces and step right to discretization of ordinary time-derivative on the right-hand side of (3.1) so that one ends up with a sequence of time-independent problems with usual Sobolev spaces. But equality (3.1) holds only for time-independent integration domains hence it needs some modification.

We consider time-dependent domain  $D(t)$  and velocity  $\mathbf{u}^B$  given in  $D(t)$  which specifies movement of  $\partial D(t)$ . We start with convective derivative of some quantity  $\phi$  in divergence form a rewrite it using the Reynolds transport theorem

$$\int_{D(t)} [(\rho\phi)' + \operatorname{div}(\rho\phi\mathbf{u})] \psi \, dV = \frac{d}{dt} \int_{D(t)} \rho\phi\psi \, dV + \int_{D(t)} \operatorname{div}(\rho\phi(\mathbf{u} - \mathbf{u}^B)) \psi \, dV \quad (3.2)$$

where we choose test function  $\psi$  so that

$$\psi' + \mathbf{u}^B \cdot \nabla \psi = 0. \quad (3.3)$$

We have a freedom to do that and it is a natural choice in the context of finite element method on a moving mesh. The right-hand side of (3.2) constitutes a material derivative term in ALE (Arbitrary Lagrangian–Eulerian) weak formulation. The reference frame arbitrariness is manifested by the arbitrariness of  $\mathbf{u}^B$  as a velocity advecting test space as well as basis functions of a Galerkin expansion of  $\phi$  and  $\psi$ .<sup>4</sup>

Divergence form  $(\rho\phi)' + \operatorname{div}(\rho\phi\mathbf{u})$  of momentum material derivative  $\rho\dot{\mathbf{u}}$  is obtained with using proper mass balance (2.1). But we rather use modified mass balance (2.29), (2.30). We are not sure whether formulation using right-hand side of (3.2) is suitable or it should be modified to be compatible with modified mass balance.

Therefore we employ standard formulation of material derivative to derive ALE formulation

$$\int_{D(t)} \rho(\phi' + \mathbf{u} \cdot \nabla \phi) \psi \, dV = \int_{D(t)} \rho \left[ \frac{D^B}{Dt} \phi + (\mathbf{u} - \mathbf{u}^B) \cdot \nabla \phi \right] \psi \, dV, \quad (3.4)$$

---

`org/blechta/dolfin`. Its inefficiency is caused by the fact that a complete serial copy of a parallel function to be projected is constructed prior to actual projection. Besides data transfer (made using file system) overhead, memory of every single process must accommodate whole projected function. This absolutely cancels an opportunity of using large amount of distributed memory to solve problems limited by memory demands.

<sup>3</sup><http://cluster.karlin.mff.cuni.cz>

<sup>4</sup>With a special choice  $\mathbf{u}^B = \mathbf{u}$  or  $\mathbf{u}^B = 0$ , the Lagrangian or Eulerian formulation is restored respectively.

where we introduce convective derivative operator  $\frac{D^B}{Dt} = \frac{\partial}{\partial t} + \mathbf{u}^B \cdot \nabla$ . Now it is not obvious how this addition of by-definition-zero term makes this ALE formulation. This becomes apparent when  $\phi(x, t)$  is expressed by Galerkin expansion

$$\phi(x, t) = \phi_i(t)\phi^i(x, t) \quad (\text{summation implied}) \quad (3.5)$$

with basis functions meeting  $\frac{D^B}{Dt}\phi^i(x, t) = 0$ . Then choosing test function  $\psi = \phi^j$  we express material derivative term as

$$\phi'_i \int_{D(t)} \rho \phi^i \phi^j dV + \phi_i \int_{D(t)} \rho (\mathbf{u} - \mathbf{u}^B) \cdot \nabla \phi^i \phi^j dV. \quad (3.6)$$

There is also another good reason for starting with standard form of material derivative  $\rho(\phi' + \mathbf{u} \cdot \nabla \phi)$  rather than divergence form  $(\rho\phi)' + \text{div}(\rho\phi\mathbf{u})$ . With  $\phi = \mathbf{u}$ , former one exhibits artificial dissipation of kinetic energy while latter supports its growth as shown by numerical experiments in [21][chapter 22]<sup>5</sup>.

## 3.2 Spatial discretization

It is well-known that the Taylor-Hood P2/P1 space and P1isoP2/P1 space on a simplicial mesh is stable discretization of the Stokes problem in Cartesian coordinates in the sense of the Babuška-Brezzi condition. Deparis [11][sections 1.3–1.5] shows that P1isoP2/P1 space is conforming to weighted Sobolev space for velocity and pressure  $(V_r \times V_z) \times P$  as defined in section 2.3 and fulfills the Babuška-Brezzi condition (given by the norms of the weighted spaces  $V_r, V_z, P$ ).

We use P2/P1 elements which are very similar to P1isoP2/P1 – in particular they have a same number of degrees of freedom, even same location of them; only shape functions are slightly different.

Let  $\mathcal{T}_h$  be a triangulation of the domain  $\Omega \cup \Lambda \cup \Delta \cup \Phi \cup \Psi$  matching the interfaces between  $\Omega, \Lambda, \Delta, \Phi, \Psi$  mutually. Then we define function spaces

$$V_h = \left\{ \mathbf{u}_h \in \mathcal{C}(\overline{\Omega \cup \Lambda \cup \Delta})^2, \mathbf{u}_h|_T \in \mathcal{P}_2(T)^2 \forall T \in \mathcal{T}_h, \mathbf{u}_h|_{\Gamma_{\Omega}^D} = 0, (u_h)_z|_{\Sigma} = 0 \right\}, \quad (3.7)$$

$$P_h = \{p_h \in \mathcal{C}(\Omega \cup \Lambda \cup \Delta), p_h|_T \in \mathcal{P}_1(T) \forall T \in \mathcal{T}_h\}, \quad (3.8)$$

$$Q_h = \left\{ \theta_h \in \mathcal{C}(\overline{\Omega \cup \Lambda \cup \Delta \cup \Phi \cup \Psi}), \theta_h|_T \in \mathcal{P}_1(T) \forall T \in \mathcal{T}_h, \theta_h|_{\Gamma_{\Phi}^D} = 0 \right\} \quad (3.9)$$

where  $\mathcal{C}(D)$  is a set of continuous functions on  $D$  and  $\mathcal{P}_n(T)$  is a set of all polynomials of degree up to  $n$  on  $T$ .

As was shown in section 2.3 we will end with viscous term integral containing irreducible  $1/r$  factor. Deparis [11][section 2.3.2] shows on example that an evaluation of such an integral analytically is numerically unstable. He states that internal nodes quadrature formula is therefore preferable. FEniCS implements the Gauss quadrature formulae of arbitrary order and estimates necessary order automatically. As this estimation ensures an exact quadrature only for polynomials, we instruct FEniCS to use degree 2 for  $1/r$  term.

---

<sup>5</sup>In [21][chapter 22] there is also shown for incompressible flows that so-called skew-symmetric form, which is average of both approaches, conserves kinetic energy. We did not investigate how this can be incorporated with a variable density.

Similar situation arises with Darcy-like forcing term with coefficient (2.23). But we do not put stress on quadrature accuracy of this term as we consider this as rather a heuristic penalty rather than accurate physics, as was discussed earlier. Nevertheless we must modify formula (2.23) to stay finite in solid phase. We adopt formula from [22]

$$S(\phi) = Cq \frac{(1 - \phi)^2}{\phi^3 + q}. \quad (3.10)$$

We observed that stability of algorithm and also velocity in mushy region is strongly dependent on values of  $C$  and  $q$ . But we are not aware of any method justifying particular values. We succeeded with values  $C = 5 \times 10^{10} \text{ Pa s m}^{-2}$  and  $q = 0.001$ .

Phase interface thickness parameter  $\epsilon$  (given as temperature difference) needs to be sufficiently large so that phase interface width is comparable at least as few cells of a mesh. This is mainly given by the latent heat term in  $c_p^{\text{eff}}$  approximating Dirac  $\delta$ -distribution. If it was approximated by too thin peak, Gauss quadrature would not be able to sample it accurately if at all. In practice we need  $\epsilon \gtrsim 1 \text{ K}$  with used spatial resolution and reached temperature gradients.

### 3.3 Temporal discretization

Let us have constant time-step  $\delta t$ . We define

$$t^n = n \delta t \quad (3.11)$$

$$\phi^n = \phi(t^n) \quad (3.12)$$

for all time-dependent quantities  $\phi$ , including domains and functions spaces.

Now we approximate  $\mathbf{u}^{\text{B}}$ -convective derivative of quantity  $\phi$  expressed by expansion (3.5) as

$$\left( \frac{\text{D}^{\text{B}} \phi}{\text{D} t} \right)^{n+1} \approx \left( \frac{\delta^{\text{B}} \phi}{\delta t} \right)^{n+1} \equiv \frac{\phi_i^{n+1} - \phi_i^n}{\delta t} (\phi^i)^{n+1}. \quad (3.13)$$

We propose a following discrete problem: find  $\mathbf{u}^{n+1}$ ,  $p^{n+1}$  and  $\theta^{n+1}$  such that

$$\mathbf{u}^{n+1} - (\mathbf{u}^{\text{D}})^{n+1} \in V_h^{n+1} \quad (3.14)$$

$$p^{n+1} \in P_h^{n+1} \quad (3.15)$$

$$\theta^{n+1} - (\theta^{\text{D}})^{n+1} \in Q_h^{n+1} \quad (3.16)$$



$$0 = \int_{\Omega^{n+1} \cup \Lambda^{n+1} \cup \Delta^{n+1}} q [\operatorname{div}(\hat{\rho}^n \mathbf{u}^{n+1}) - \alpha^n] \, dV \quad \forall q \in P_h^{n+1} \quad (3.17)$$

$$0 = \int_{\Omega^{n+1} \cup \Lambda^{n+1} \cup \Delta^{n+1}} \left[ \rho^{n+1} \left( \left( \frac{\delta^B \mathbf{u}}{\delta t} \right)^{n+1} + \nabla \mathbf{u}^{n+1} (\mathbf{u}^{n+1} - (\mathbf{u}^B)^{n+1}) \right) \cdot \mathbf{v} \right. \\ \left. - p^{n+1} \operatorname{div} \mathbf{v} + \mu^{n+1} (\nabla \mathbf{u}^{n+1} + (\nabla \mathbf{u}^{n+1})^\top) \cdot \mathbf{v} \right. \\ \left. - \rho^{n+1} \mathbf{g} \cdot \mathbf{v} + S^{n+1} \mathbf{u}^{n+1} \cdot \mathbf{v} \right] \, dV \quad \forall \mathbf{v} \in V_h^{n+1} \quad (3.18)$$

$$0 = \int_{\Omega^{n+1} \cup \Lambda^{n+1} \cup \Delta^{n+1} \cup \Phi^{n+1} \cup \Psi^{n+1}} \left[ \rho^{n+1} \left( (c_p^{\text{eff}})^{n+1} \left( \frac{\delta^B \theta}{\delta t} \right)^{n+1} + (c_p)^{n+1} (\mathbf{u}^{n+1} - (\mathbf{u}^B)^{n+1}) \cdot \nabla \theta^{n+1} \right) \eta \right. \\ \left. + \kappa^{n+1} \nabla \theta^{n+1} \cdot \nabla \eta \right] \, dV \quad \forall \eta \in Q_h^{n+1}. \quad (3.19)$$

Interfacial velocity condition on  $\Sigma^{n+1} = \partial\Omega^{n+1} \cap \partial\Lambda^{n+1}$  is treated explicitly as a Dirichlet condition (3.14). If we choose  $q = 1$  in  $\Omega^{n+1}$  and  $q = 0$  elsewhere in mass balance (3.17) we get necessary condition

$$u_z^{n+1}|_{\Sigma^{n+1}} \int_{\Sigma^{n+1}} \hat{\rho}^n|_{\Omega^{n+1}} \, dS = \alpha^n |\Omega^{n+1}|. \quad (3.20)$$

Treating density and an approximation of its time-derivative in mass balance (3.17) explicitly must be accomplished by asserting necessary condition (3.20). Another possibility would be to treat both these quantities implicitly and enforce a necessary condition by Lagrange multiplier.

Calculation of quantity  $\alpha_n$  using a formula  $\alpha \approx -\rho'$  would be cumbersome on deforming mesh. Moreover we can turn to the first purpose of introducing pseudo-incompressibility constraint (2.29) – enforcement of total mass conservation of  $\text{PbCl}_2$  in  $\Omega$ . After a solution of the discrete problem (3.14)–(3.19) we end up with density  $\rho^{n+1}$  given merely by temperature  $\theta^{n+1}$  and violating total mass conservation in  $\Omega^{n+1}$ . Afterwards mesh is very slightly deformed such that surface  $\Sigma^{n+1}$  moves precisely such that

$$\int_{\Omega^{n+2}} \hat{\rho}^{n+1} \, dV = m_{\text{PbCl}_2}^0 \quad (3.21)$$

where  $\hat{\rho}^{n+1}$  is  $\rho^{n+1}$  convected by this movement and  $m_{\text{PbCl}_2}^0$  is mass of  $\text{PbCl}_2$ . Before this correction we have solution with an error in total mass of  $\text{PbCl}_2$  and after it we conversely have fields with correct total mass but not fulfilling field equations (3.17)–(3.19). Mentioned deformation of a mesh and whole algorithm will be precisely presented hereafter.

Let  $\mathbf{d}^n$  is displacement field of this deformation. Having finished field compu-

tation (3.14)–(3.19) we set

$$\mathbf{d}^{n+1,*} := 0, \quad (3.22)$$

$$\hat{\rho}^{n+1,*} := \rho^{n+1}, \quad (3.23)$$

$$\Omega^{n+1,*} := \Omega^{n+1}, \quad (3.24)$$

$$\Lambda^{n+1,*} := \Lambda^{n+1}, \quad (3.25)$$

$$\Sigma^{n+1,*} \equiv \partial\Omega^{n+1,*} \cap \partial\Lambda^{n+1,*} \quad (3.26)$$

and perform iterative procedure

$$d_z^{n+1,*}|_{\Sigma^{n+1,*}} := d_z^{n+1,*}|_{\Sigma^{n+1,*}} + \frac{\int_{\Omega^{n+1,*}} \hat{\rho}^{n+1,*} dV - m_{\text{PbCl}_2}^0}{\int_{\Sigma^{n+1,*}} \hat{\rho}^{n+1,*}|_{\Omega^{n+1,*}} dS}, \quad (3.27)$$

$$\text{deform mesh of } \Omega^{n+1,*} \cup \Lambda^{n+1,*} \text{ with constraint (3.27),} \quad (3.28)$$

$$\text{convect } \hat{\rho}^{n+1,*} \text{ with this displacement } \mathbf{d}^{n+1,*} \quad (3.29)$$

until mass-conservation constraint (3.21) is met with some precision. Finally we set

$$\Omega^{n+2} := \Omega^{n+1,*}, \quad (3.30)$$

$$\Lambda^{n+2} := \Lambda^{n+2,*}, \quad (3.31)$$

$$\hat{\rho}^{n+1} := \hat{\rho}^{n+1,*}, \quad (3.32)$$

$$(\mathbf{u}^B)^{n+2} := \frac{\mathbf{d}^{n+1,*}}{\delta t}, \quad (3.33)$$

$$(u_z^D)^{n+2}|_{\Sigma^{n+2}} := (u_z^B)^{n+2}|_{\Sigma^{n+2}}, \quad (3.34)$$

$$\alpha^{n+1}|_{\Omega^{n+2}} := \frac{(u_z^D)^{n+2}|_{\Sigma^{n+2}} \int_{\Sigma^{n+2}} \hat{\rho}^{n+1}|_{\Omega^{n+2}} dS}{|\Omega^{n+2}|}, \quad (3.35)$$

$$\alpha^{n+1}|_{\Lambda^{n+2}} := -\frac{(u_z^D)^{n+2}|_{\Sigma^{n+2}} \int_{\Sigma^{n+2}} \hat{\rho}^{n+1}|_{\Lambda^{n+2}} dS}{|\Lambda^{n+2}|}, \quad (3.36)$$

$$\alpha^{n+1}|_{\Delta^{n+2}} := 0. \quad (3.37)$$

Step (3.29) is do-nothing operation in context of finite elements as basis functions are convected automatically with moving mesh vertices and expansion coefficients are kept untouched. We note that procedure (3.27)–(3.29) does not converge in one iteration because numerator in (3.27) approximates rather  $\delta t \int_{\Omega} \frac{D^B \rho}{Dt} dV$  than  $\delta t \int_{\Omega} \rho' dV$ . We also note that all the surface integrals in (3.27) and (3.35) are equal (for fixed timestep  $n$ ).

Up to now we were talking about mesh displacement  $\mathbf{d}^n$  and derived reference frame velocity  $(\mathbf{u}^B)^n$  related to the movement of surface  $\Sigma^n$ . Now we remind a reader that there is another movement given by uniformly pulling rigid domains  $\Omega^n \cup \Omega^n$ ,  $\Lambda$ ,  $\Psi$  and  $\Phi$  downwards. Analogically this deforms domain  $\Delta^n$  with displacement  $\mathbf{d}^{n+1}$  and defines reference frame velocity  $(\mathbf{u}^B)^{n+1} = \mathbf{d}^{n+1}/\delta t$  and no-slip Dirichlet condition representant  $(\mathbf{u}^D)^{n+1} = (\mathbf{u}^B)^{n+1}$ , both given in domain  $\Delta^{n+1}$ .

## 3.4 Mesh

We choose mesh generator Triangle [36] to produce the constrained Delaunay triangulation. This is a generalization of the Delaunay triangulation that forces

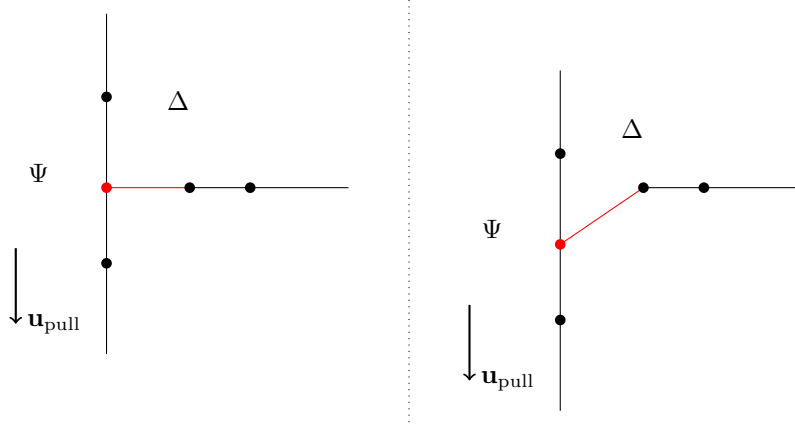


Figure 3.1: Schematic illustration of the issue with incompatibility of displacement  $\mathbf{d}$  at a red vertex. We simply resolve this by choosing  $\mathbf{d} = \delta t \mathbf{u}_{\text{pull}}$  in  $\overline{\Psi}$ . This yields unwanted movement of a red edge as a side-effect. This tiny *growth* of domain  $\Delta$  is ignored as it represents negligible error.

location of some segments. In our case a requested triangulation of domain  $\Omega \cup \Lambda \cup \Delta \cup \Phi \cup \Psi$  is supposed to be constrained by all the boundaries  $\partial\Omega$ ,  $\partial\Lambda$ ,  $\partial\Delta$ ,  $\partial\Phi$  and  $\partial\Psi$ . For the algorithm used by Triangle reader is referred to [37].

Our input to Triangle is parametrized by

- vertical coordinate  $h$  of a bottom point of  $\overline{\Omega}$ ,
- vertical coordinate  $H$  of surface  $\Sigma$ .

With  $h$ ,  $H$  set to all our use cases Triangle had no problem producing a quality triangulations with angles bounded from below by  $34^\circ$  and area of triangles bounded by  $10^{-7} \text{ m}^2$  in  $\Omega$  and  $10^{-6} \text{ m}^2$  in the rest of the domain. These meshes typically have about 19,000 vertices and 36,000 triangles.

We now explain how a mesh is deformed. First of all mesh movement is precisely described by displacement of its every vertex. Thus there is one-to-one correspondence between this displacement and piece-wise linear, continuous finite-element vector function. We must remember that we deform a mesh for two purposes – at first, conservation of mass in  $\Omega$  and at second, pulling rigid domains  $\Omega \cup \Lambda$ ,  $\Phi$  and  $\Psi$  downwards.

We decided to realize former movement by merely moving vertices lying on  $\Sigma$  according to the procedure for conservation of mass in  $\Omega$  described in the end of the previous section 3.3 and keep rest of vertices still. This is of course possible when this displacement is small compared to cell size so that it can be repeated for several time-steps before remeshing is needed.

Latter movement  $\mathbf{d}$  is given by the pulling velocity  $\mathbf{d} = \delta t \mathbf{u}_{\text{pull}}$  in domains  $\overline{\Omega \cup \Lambda}$ ,  $\overline{\Phi}$  and  $\overline{\Psi}$ . We extend this harmonically in  $\Delta$  subject to zero Dirichlet condition for normal component and homogeneous Neumann condition for tangential condition on  $\partial\Delta \setminus (\partial\Phi \cup \partial\Psi)$ . This combination of movement is not fully compatible which is illustrated and resolved in Figure 3.1. Resulting displacement (divided by time-step) contributes to reference-frame velocity  $\mathbf{u}^B$  and Dirichlet condition  $\mathbf{u}^D$  in  $\Delta$ . In the rest of the domain we forget this contribution as motion is inertial.

Both these motions cannot deform a mesh indefinitely. When deformation accumulated through consecutive time-steps would be too large it would alter mesh topology. In practice deformation must be limited much more to ensure stability and/or accuracy of the finite element solution algorithm. We watch ratio of inscribed circle radius to circumscribed circle radius of every triangle. When minimum over all triangles of the radius ratio decreases by factor 0.9 we step to remeshing. We just create a new mesh using Triangle and current values of parameters  $h$  and  $H$  and project old fields to the new mesh. For details regarding mesh quality measures (including radius ratio) reader is referred to [38].

### 3.5 Solution of field equations

Field equations (3.14)–(3.19) represents non-linear problem. FEniCS provides an implementation of the Newton method for solution of such a system. Moreover, an automatic symbolic differentiation is available so user does not need to perform an error-prone calculation of a system Jacobian. Resulting linear system of algebraic equations can be solved by many external state-of-the-art libraries. We use MUMPS (MULTifrontal Massively Parallel sparse direct Solver) which is an implementation of multifrontal algorithm [3] for computing LU or Cholesky decomposition of a sparse matrix. We have chosen LU solver because of its robustness enabling us to focus on other parts of algorithm. Of course usage of more efficient iterative solvers suggests itself to enable computations on finer meshes and with smaller  $\epsilon$ . But this would need to develop a suitable preconditioning algorithm as standard algebraic preconditioners often perform poorly on coupled problems.

Now, at the end of the chapter we briefly present algorithm 1 for numerical solution of our problem. We remark that as an initial condition we take stationary solution of field equations (3.14)–(3.19) with  $\delta t = \infty$ . With present, tuned settings it can be computed using merely slight algebraic underrelaxation. This ruins quadratic convergence of the Newton method but still requires negligible computational effort compared to whole time-stepping.

```

prepare initial mesh;
compute initial condition;
while some liquid PbCl2 remains do
  if mesh quality is poor then
    | create new mesh and project fields onto it;
  end
  pull rigid domains  $\Omega \cup \Lambda$ ,  $\Phi$ ,  $\Psi$  downwards;
  smooth mesh harmonically in  $\Delta$ ;
  set reference frame velocity  $\mathbf{u}^B$  and no-slip velocity  $\mathbf{u}^D$  in  $\Delta$ ;
  move vertices on  $\Sigma$  so that mass in  $\Omega$  is conserved;
  set reference frame velocity  $\mathbf{u}^B$  and no-slip velocity  $\mathbf{u}^D$  in  $\Omega$ ,  $\Lambda$ ;
  solve field equations (3.14)–(3.19);
end

```

**Algorithm 1:** Algorithm of entire calculation.

## 4. Results

We performed numerical calculations for all of four temperature profiles and pulling rates  $u_{\text{pull}} = 0.9, 2.7, 5.4$  mm/h. Used time-steps and width of diffuse interface are shown in table 4.1. This means that we did five calculations for every of four temperature profiles.

Computations with higher pull-rates would be also desirable. Problem is that they would require even smaller time-steps, not only from stability and accuracy reasons, but also because increased velocity of mesh deformation requires a more frequent remeshing. Between two remeshings at least one time step is required but rather more for better dissipation of numerical error introduced by a projection.

Chosen interface widths  $\epsilon$  are limited by fineness of a mesh. In fact we performed all the calculations on meshes of approximately same fineness because we are limited by cubic scaling of the LU method. Two-times finer mesh in both spatial dimensions means four-times more degrees of freedom and 64-times more work of LU solver for single time-step. In figure 4.1 there is one of the most extreme temperature gradients achieved when a phase interface is as thick as only few mesh triangles. This is practically limiting case for value of  $\epsilon$  because quadrature of approximate Dirac- $\delta$  latent heat may be becoming quite inaccurate with smaller  $\epsilon$ .

One can observe in figure 1.3 that temperature profiles are decreasing with height in top parts of the furnace. In the beginning of the growth process when ampoule is at the highest position, protective atmosphere and possibly also top part of the melt is unstably stratified. This possibly enhances stiffness of the problem. In fact we observed during the development of the numerical algorithm strong instability under such a conditions, particularly when no protective atmosphere was considered yet and ampoule was full of  $\text{PbCl}_2$ . We resolved this by introducing protective atmosphere, refining a mesh and possibly also by other tweaks and bugfixes. The former evidences somewhat that under these conditions  $\text{PbCl}_2$  is more susceptible to some kind of instability than protective atmosphere or even air in the furnace which withstands unstable stratification. It is also possible that turbulence is induced in top parts of the melt with high ampoule positions. It cannot be easily decided using a priori dimensional analysis as classical Grashof and Rayleigh number criteria applies usually to quite different situations. We are not aware of such a result with similar geometry and heat conditions. From a crystal growth perspective, turbulence occurring far from a phase interface would not be harmful to crystal quality. Possibly it would enhance it by increased dissolution of chlorination agent.

$u_{\text{pull}}$ [mm/h]	$\delta t$ [s]	$\epsilon$ [K]
0.9	120	5
0.9	120	2
0.9	120	1
2.7	120	5
5.4	60	5

Table 4.1: Used numerical parameters.

profile	$h^0$ [m]
TP1	0.295
TP2	0.295
TP3	0.290 <sup>a</sup>
TP4	0.275

Table 4.2: Used initial values  $h^0$  of ampoule position  $h$ .

---

<sup>a</sup>As only exception, calculation with TP3,  $\epsilon = 2$  was started with  $h = 0.2901$  m because of a minor issue with poor mesh deformation which can happen accidentally.

Still we are not able to obtain an initial steady state for ampoule positioned too high and we are forced to start all the calculations with positions such that cone of the ampoule contains a little amount of a solid. Such a situation is depicted in figure 4.1. We state used initial positions in table 4.2. For depth of  $\text{PbCl}_2$  (i.e. distance of  $\Sigma$  from bottommost point of ampoule)  $H$  we choose initial condition  $H^0 = 8$  cm which corresponds in all cases to  $\text{PbCl}_2$  mass  $m_{\text{PbCl}_2} = (164 \pm 1)$  g.

We also calculated steady-state solution for many values of  $h$  and all the set-ups given above. We do this within transient computations to take advantage of having all the infrastructure prepared and having transient solution as good starting point for Newton iteration of stationary problem. It has not been tuned as precisely as transient computation so it does not converge every time but this does not matter.

Newton iteration for transient solution also diverges for some cases solved during solidification of the topmost part of  $\text{PbCl}_2$ . It is possibly caused by interaction of the two special features of the algorithm – treatment of interface  $\Sigma$  and treatment of the solid-liquid interface – which we did not tune anyhow for this event. Anyway, we are not interested a much in the solution around this event.

We computed viscous powers in  $\Omega$ ,  $\Lambda$  and  $\Delta$  every time-step. Total work done by viscosity during whole process ranges from ca. 7 mJ to 200 mJ depending practically only on temperature profile and proportionally on a duration of the process (given by pull-rate). In particular the most significant is power in  $\Delta$

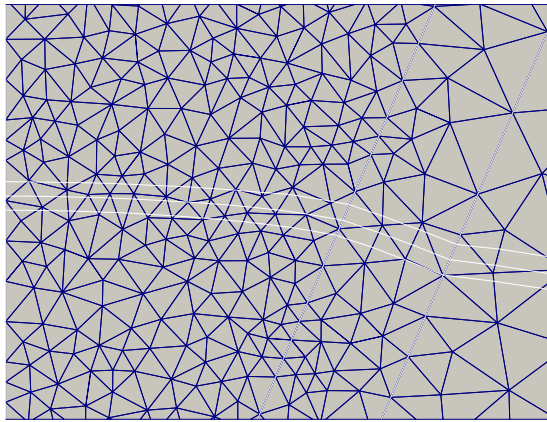


Figure 4.1: Mesh and isotherms  $\theta_m - \epsilon$ ,  $\theta_m$ ,  $\theta_m + \epsilon$  computed with profile TP1 and  $\epsilon = 1$ . Oblique white lines represent a cone of the ampoule. This is a situation near the beginning of the growth process when phase interface is located within conical part of the ampoule.

ranging ca. from 32 nW to 680 nW according to temperature profile and ampoule position. Viscous power in  $\Omega$  and  $\Lambda$  are ca. 2–3 and 10 orders of magnitude smaller respectively. This shows that we did a correct assumptions when neglecting viscous power in energy balance.

In figure 4.2 we present velocity field at various parts of the system. In figure 4.2a there is typical air flow above ampoule. In figure 4.2b and 4.2d one can see how a melt and a protective atmosphere driven by buoyancy induces a small wake in the atmosphere required for the compatibility requirement on interfacial velocities. Figure 4.2b also shows proportions of a velocity field on whole ampoule. Typical flow pattern in a melt is well visible in figures 4.2c, 4.2e and 4.2f. Figures 4.2b, 4.2e and 4.2f also shows a velocity wiggle on interface. Possibly it is caused by poor set-up of constants  $C$  and  $q$  of Darcy-like forcing but we are quite satisfied with current working status. Finally figure 4.2g shows a simple up-and-down flow pattern of furnace air around ampoule holder. Flow in the gap between ampoule and furnace wall is much slower, maybe also because of numerical boundary layer due to insufficient mesh resolution.

Evolution of fields is somewhat visible in figures 4.3–4.6 but we encourage reader to explore animations on the enclosed optical disk. Apart from better temporal resolution, all the computed cases are available. In subsequent sections we will present some comparison between calculations and also temperature measurements described in section 1.3. Some presented figures are plotted as dependence on ampoule position  $h$  instead of time. This is natural scaling for comparison of calculations with different pull-rates  $u_{\text{pull}}$ . In these figures we then unusually let the variable  $h$  to decrease from the left to the right which resembles increasing time.

## 4.1 Shape of phase interface

As we stated previously, shape of phase interface is crucial to crystal quality. We would like to evaluate dependence of the shape on used temperature profile and pulling rate.

One could try to directly compute curvature  $\zeta$  of melting point isotherm from normal unit vectors  $\mathbf{n}$  of isotherms using formulas

$$\zeta = \text{div } \mathbf{n}, \quad (4.1)$$

$$\mathbf{n} = \frac{\nabla \theta}{|\nabla \theta|}. \quad (4.2)$$

But this cannot be done directly with used finite element space because normals  $\mathbf{n}$  are piece-wise constant and discontinuous. Therefore  $\text{div } \mathbf{n}$  has no good meaning as curvature either globally or locally on element. One could project  $\mathbf{n}$  to some  $H(\text{div})$ -conforming space and then calculate curvature using (4.1). We tried this on simple test cases with piece-wise linear Raviart-Thomas elements on same mesh. It did not work satisfactorily as oscillations were induced near boundary and its derivatives did not converge with mesh-step size. The issue may be possibly solved by using different mesh for target space of normal  $\mathbf{n}$ . Another possibility may be to use higher-order temperature space so that  $\mathbf{n}$  is not piece-wise constant but then it is not obvious how to treat (4.2) as right-hand side contains square root of polynomial in its denominator.

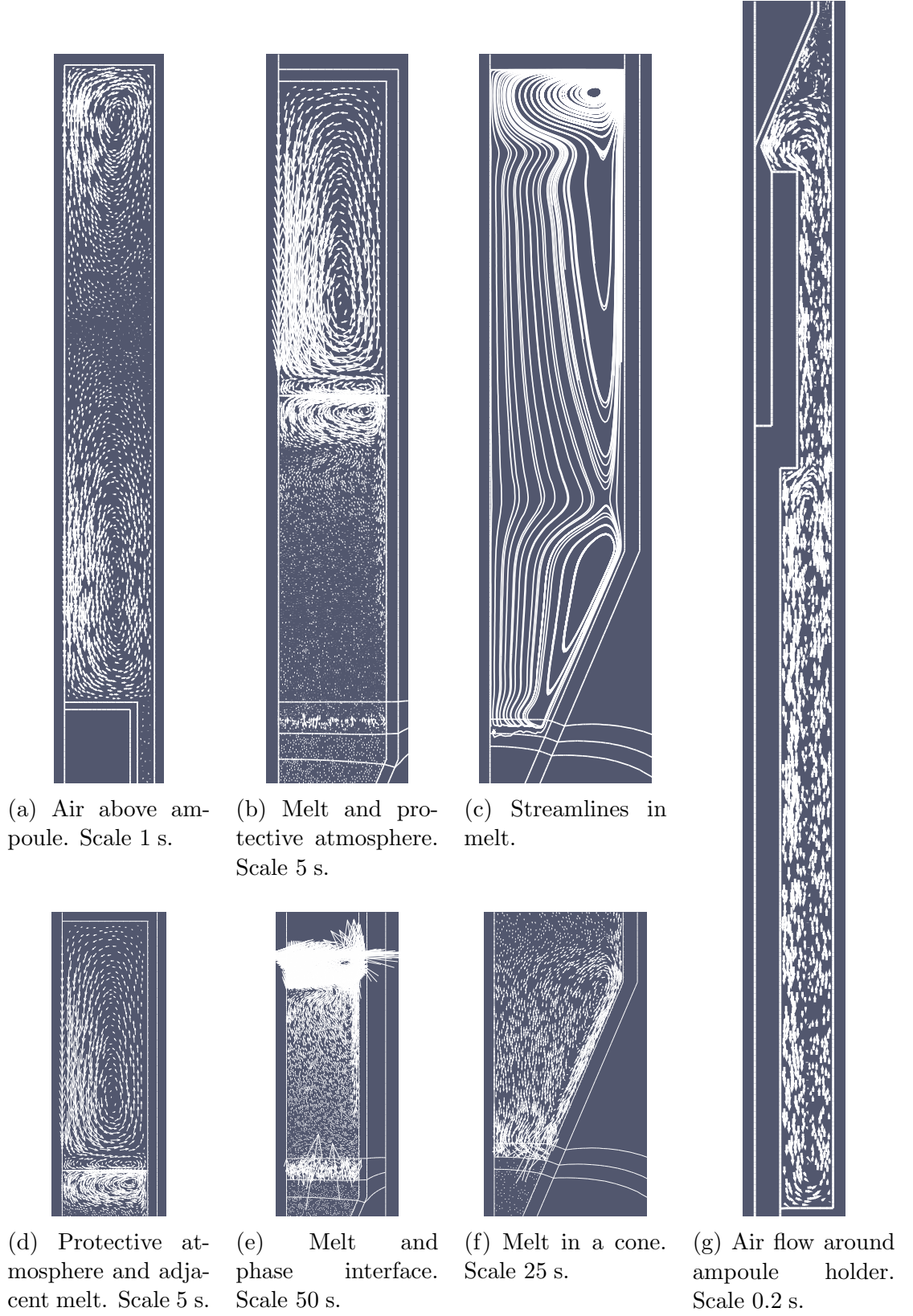


Figure 4.2: Velocity in various locations of the system. Computed with profile TP2,  $u_{\text{pull}} = 0.9$  mm/h,  $\epsilon = 2$  K at  $t = 49$  h except (c) and (f) at  $t = 19$  h. Scaling factors are given, which say how much time is needed for a flow to travel a distance given by arrow length.

*Erroneously, isotherms corresponding to  $\epsilon = 5$  K are plotted on figure 4.2. Producing this figure was lengthy and not automated process and the error was detected too late. This publishing mistake is definitely not an issue as keen reader can very simply imagine correct isotherms.*



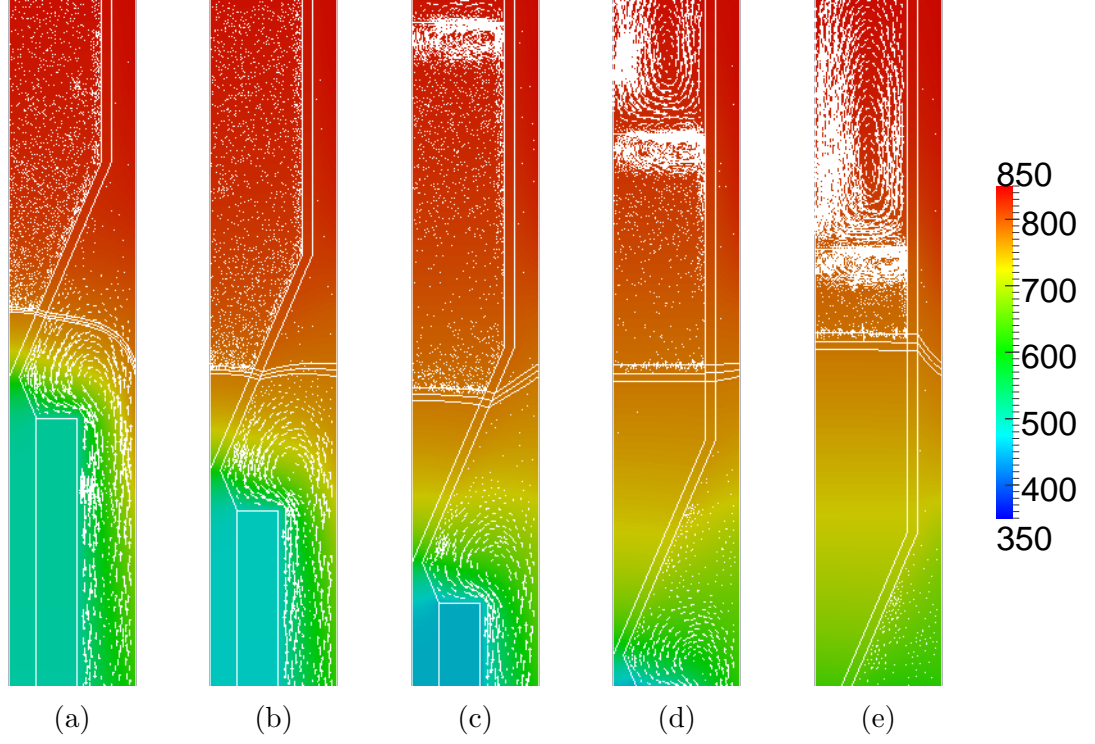


Figure 4.3: Temperature and velocity in a region near phase interface for TP1,  $u_{\text{pull}} = 0.9$  mm/h,  $\epsilon = 2$  at  $t = 0, 15, 30, 45, 60$  h. Velocity scale 5 s in ampoule and 0.1 s in furnace. Isotherms  $\theta_m, \theta_m \pm \epsilon$ . Temperature in color.

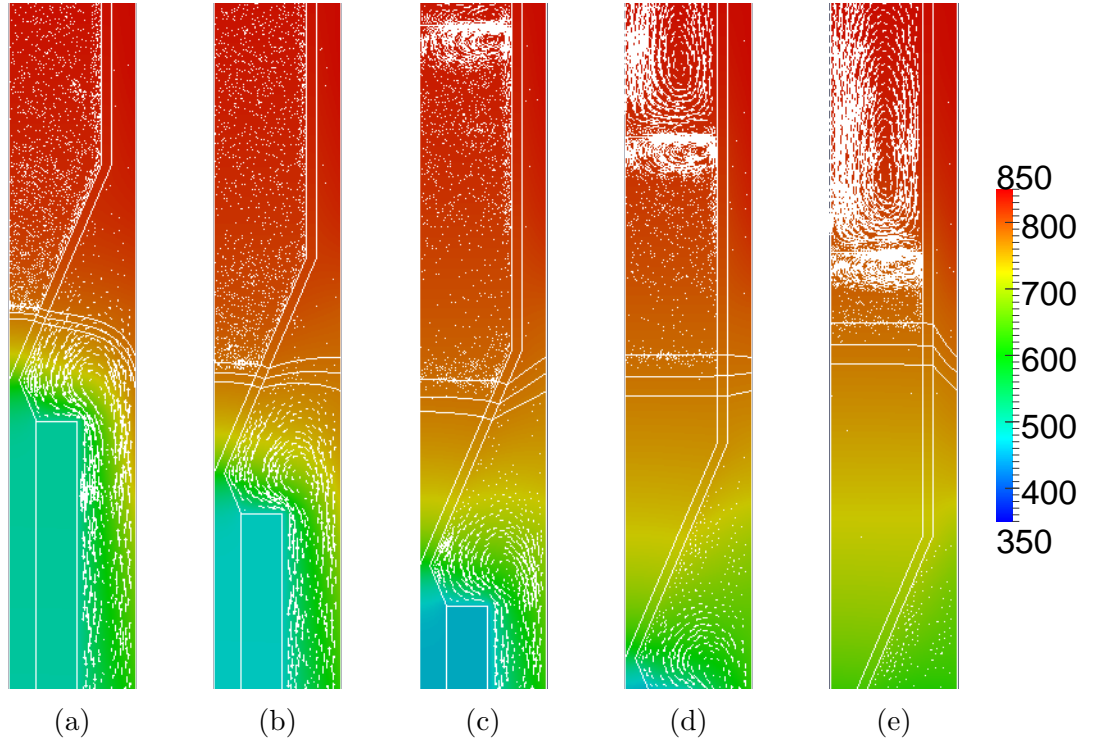


Figure 4.4: Temperature and velocity in a region near phase interface for TP1,  $u_{\text{pull}} = 0.9$  mm/h,  $\epsilon = 5$  at  $t = 0, 15, 30, 45, 60$  h. Velocity scale 5 s in ampoule and 0.1 s in furnace. Isotherms  $\theta_m, \theta_m \pm \epsilon$ . Temperature in color.

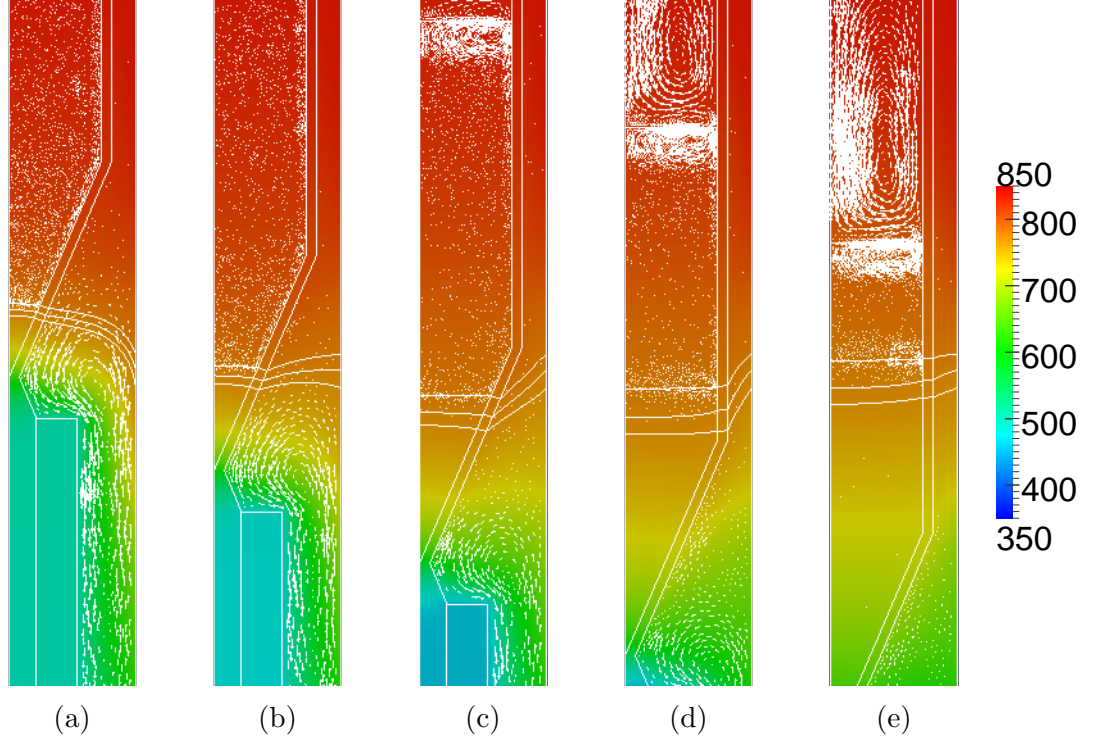


Figure 4.5: Temperature and velocity in a region near phase interface for TP1,  $u_{\text{pull}} = 5.4$  mm/h at  $t = 0, 2.5, 5, 7.5, 10$  h. Velocity scale 5 s in ampoule and 0.1 s in furnace. Isotherms  $\theta_m, \theta_m \pm \epsilon$ . Temperature in color.

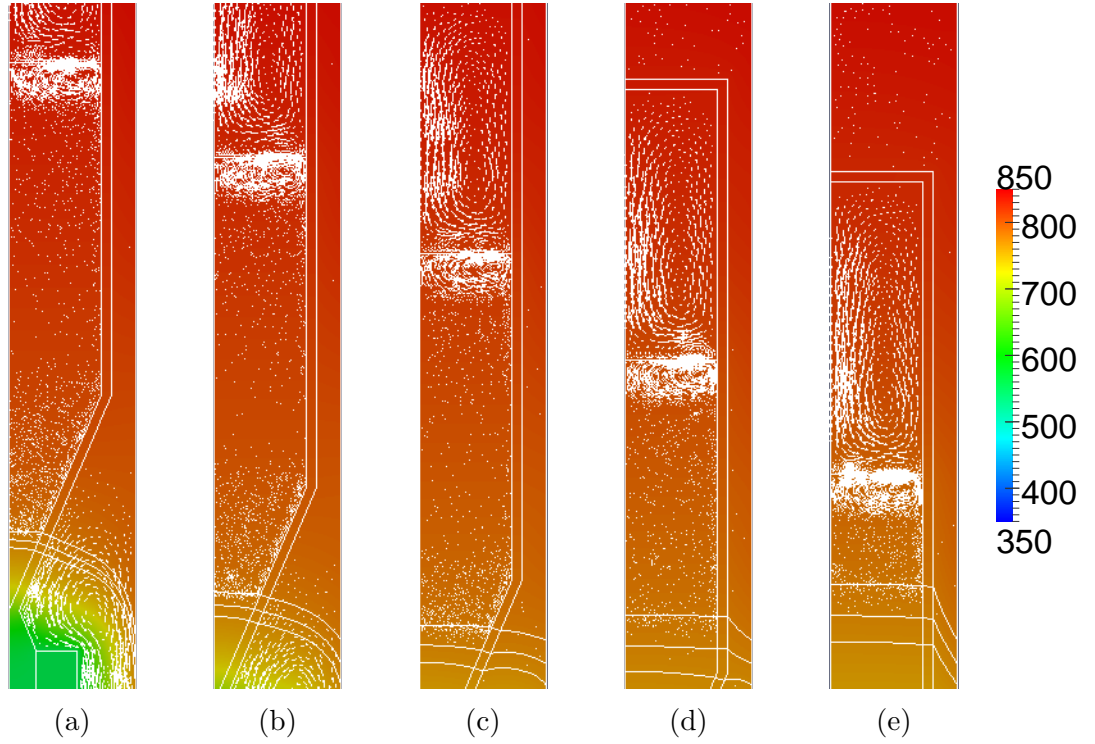


Figure 4.6: Temperature and velocity in a region near phase interface for TP4,  $u_{\text{pull}} = 0.9$  mm/h,  $\epsilon = 5$  at  $t = 15, 30, 45, 60, 75$  h. Velocity scale 5 s in ampoule and 0.1 s in furnace. Isotherms  $\theta_m, \theta_m \pm \epsilon$ . Temperature in color.

We therefore stick to looking on plots of isotherms by naked eye although we are quite frustrated by our lack of quantitative method. Hereafter we will give plots of velocity and temperature fields with consistent scaling between different figures unless otherwise stated. Color legend for temperature is given near figures. Isotherms corresponds to  $\theta = \theta_m \pm \epsilon$ . Arrows correspond to velocity scaled by factors 5 s and 0.1 s in the ampoule (both melt and protective atmosphere) and in the furnace (air) respectively.

We observe that with all used set-ups, interface is safely convex in the conical part of the ampoule and it tends to become planar or even concave when passing into cylindrical part of the ampoule as seen in figures 4.3d, 4.4d and 4.5d. In particular higher pulling rates induce concave interface while low pull-rate  $u_{\text{pull}} = 0.9$  mm/h supports planar or possibly slightly concave interface as seen by comparison of figures 4.4 and 4.5. Profile TP4 helps the best to keep interface convex as seen in figures 4.6d and 4.6e.

Analysis on a position of the interface will be given in section 4.3.

## 4.2 Comparison with steady states

Knowing how accurately are transient states approximated by steady states is desirable from a few reasons. Generally one may exploit such an accuracy for a simplification of numerical simulations. We are specially interested in the issue as available experimental data are measured on the steady system and we would like to know how far these are from actual growth conditions. We will focus to the experimental data in the next chapter. Last but not least, understanding this matter is closely related to considerations of crystal quality.

At first we can take a look to figure 4.7 which clearly shows that with increasing pull-rate crystallization is more lagging behind slower or steady states. In we figures 4.8–4.10 we show  $L^2$  average of temperature difference between steady and transient solution. We can see a correspondence to a previous statement – difference significantly increases with pull-rate. *Gaps* in figures are caused by an excessive stiffness of the steady problem so that Newton solver does not converge. We observe general trend that this happens more often with small  $\epsilon = 1$  K (see figure 4.9a) and with high pull-rate  $u_{\text{pull}} = 5.4$  mm/h (see figure 4.10b). This holds generally and reader can check similar figures for other cases on enclosed optical disk. Exception is profile TP4 which *behaves well* even with the highest pull-rate – see figure 4.8.

First bump or wiggle in figure 4.9b and 4.10a occurs at a moment where phase interface passes from a conical to a cylindrical part of the ampoule. Second one corresponds happens when all  $\text{PbCl}_2$  is crystallized. Figure 4.8 does not possess second one as calculation was finished before this event. This happened for some calculations because it is not a priori easy to predict needed time for given an initial ampoule position as evidenced by small derivative in figure 4.7 on the beginning of the process. Conversely it is difficult (probably also in laboratory) to find the bottommost ampoule position such that it will melt all  $\text{PbCl}_2$ . This is best observed on the beginning phases of enclosed animations when isotherms induced by a temperature profile moves almost with an ampoule and changes their slope to almost vertical with increasing  $h$  as shown in figure 4.6a. Therefore crystal grower must select ampoule position with a safe margin so that all

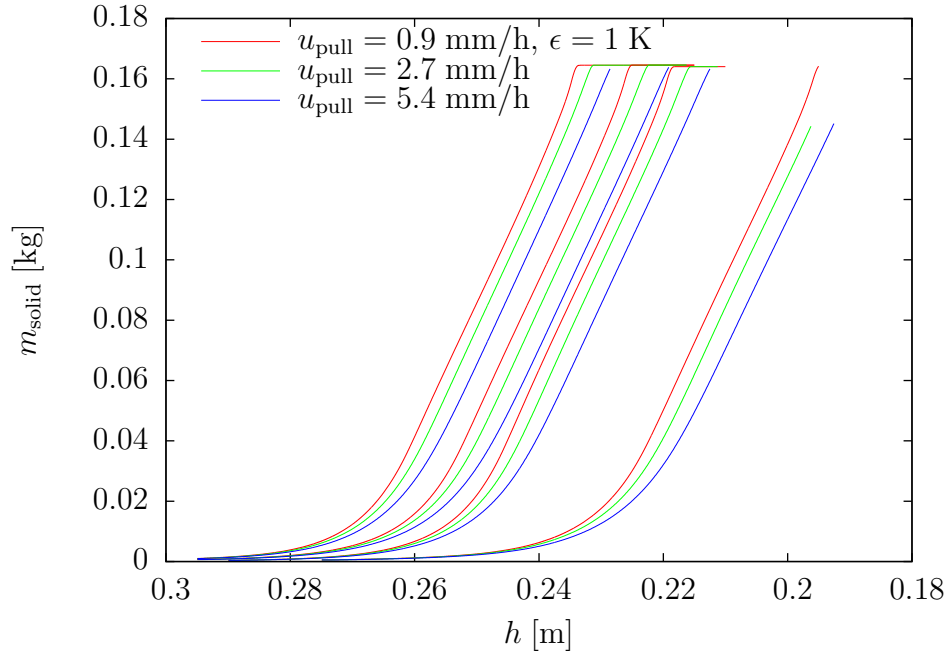


Figure 4.7: Evolution of mass of solid  $\text{PbCl}_2$  during growth process. Each triplets of red, green and blue line corresponds to profile TP1, TP2, TP3 and TP4 from left to right. Note that we do not show curves for various  $\epsilon$  as these are practically same.

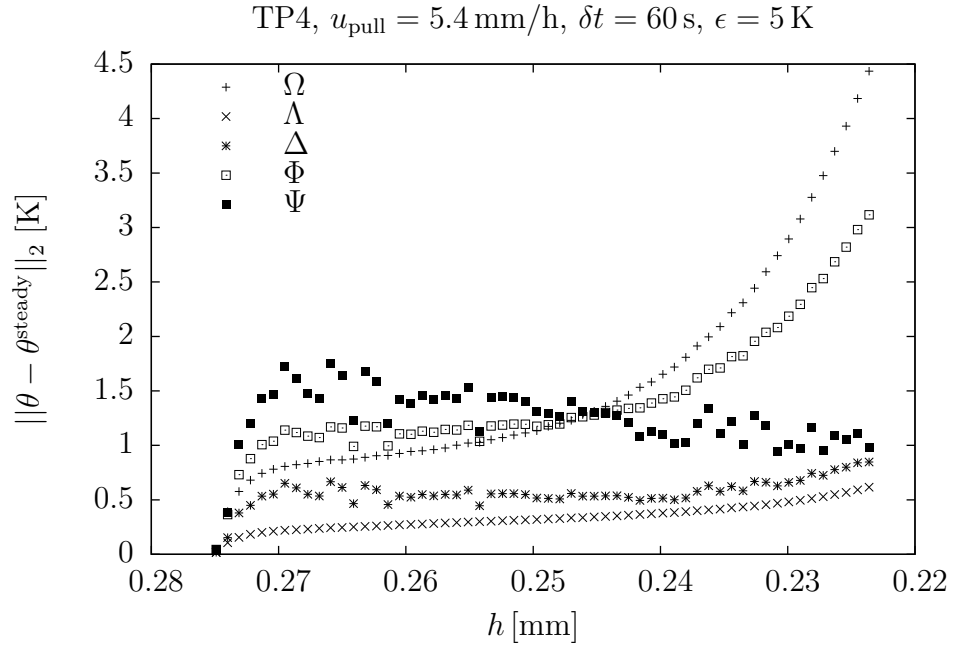


Figure 4.8: Comparison of transient and steady solutions. Plotted quantity is  $L^2$  norm of temperature difference in respective domain normalized to unit volume.

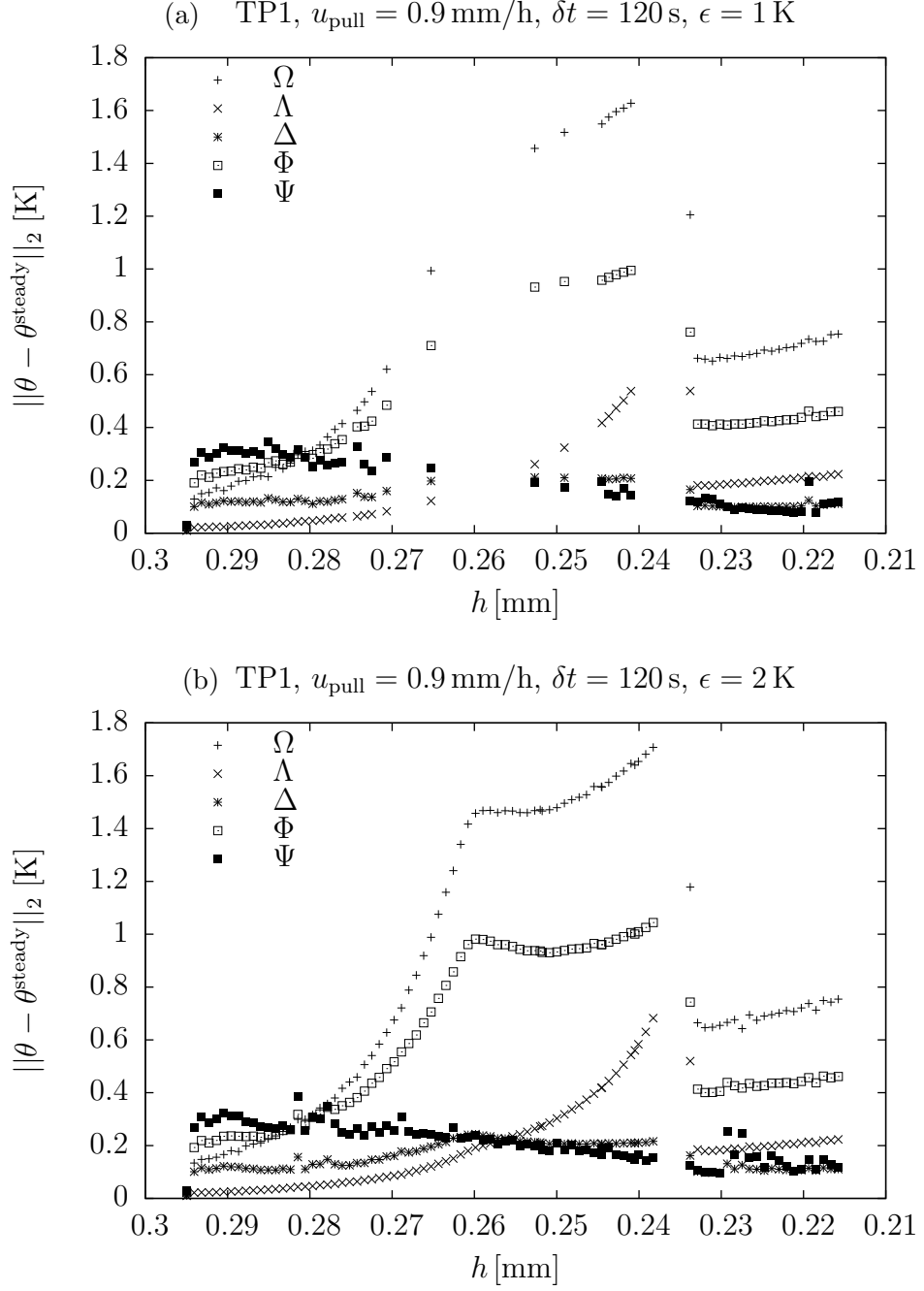


Figure 4.9: Comparison of transient and steady solutions. Plotted quantity is  $L^2$  norm of temperature difference in respective domain normalized to unit volume.

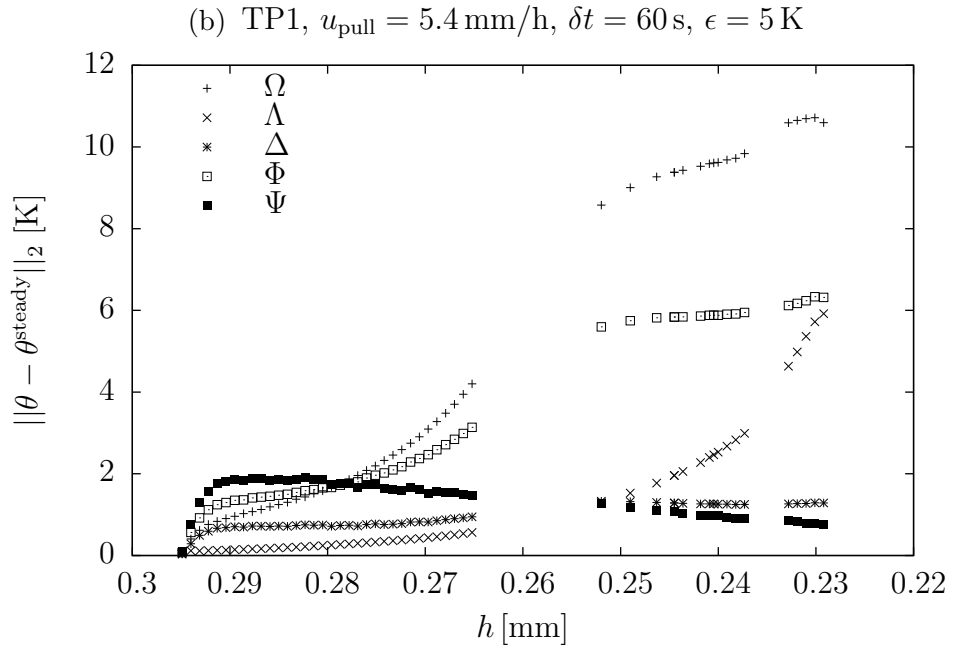
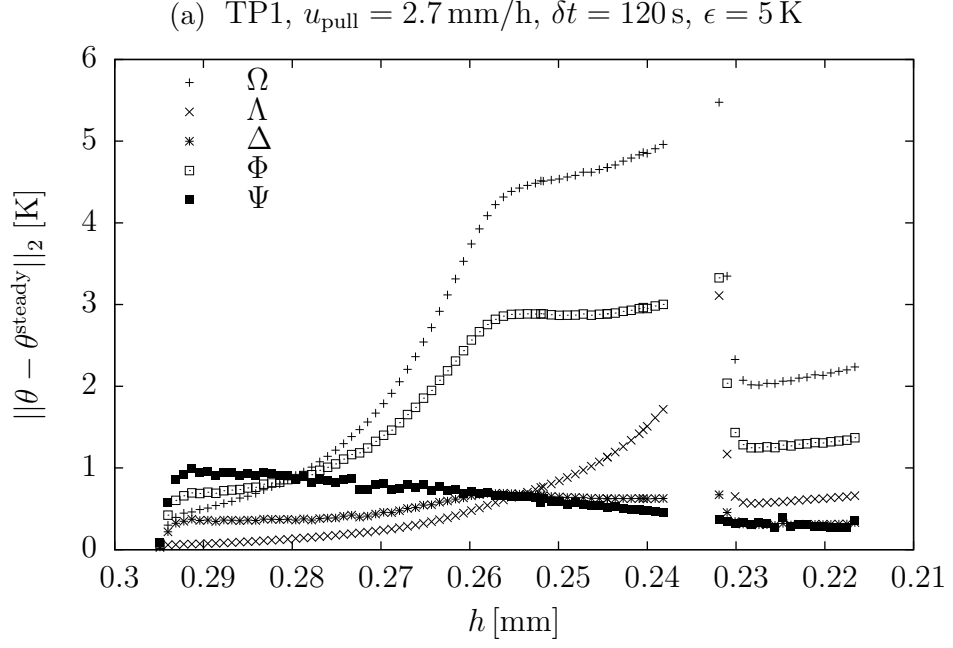


Figure 4.10: Comparison of transient and steady solutions. Plotted quantity is  $L^2$  norm of temperature difference in respective domain normalized to unit volume.

poly-crystalline material is definitely melted. This unnecessarily prolongs growth process. Possible remedy could be to use higher pull-rates in the beginning and gradually slow them to usual values so that dependence (mass) growth rate would be rather to linear in comparison to curves in 4.7.

### 4.3 Comparison with experimental data

In section 1.3 we described experimental arrangement used for a measurement of temperature field in ampoule. Now we step to comparison of experimental data obtained by Král [20] with computations of our numerical model. We simply evaluate our solutions at position of capillaries and ampoule position for which experimental data were measured. We remark that our solution is axisymmetric so it plays no role that capillaries depicted in figure 1.4 do not lie in a common plane. Note also that for all temperature profiles and for three distinct positions of ampoule steady-state temperature fields in capillaries were measured. In all these cases phase interface was located in cylindrical part of the ampoule and being crossed by capillaries.

On the enclosed optical disk reader can find figures comparing numerical data to all available experimental data. We now present only examples to reach some conclusions. We compare also to transient solutions hence for slow pull-rate  $u_{\text{pull}} = 0.9 \text{ mm/h}$  we pick only  $\epsilon = 1 \text{ K}$  as others are almost negligibly close. In a same manner we take stationary solution with  $\epsilon = 2 \text{ K}$  for comparison with experiment.<sup>1</sup>

In figures 4.11–4.14 we show comparison of calculated and experimental values. First of all, calculated data seems to be very consistent. A lag behind steady solution increases with pull-rate. The highest employed pull-rate  $u_{\text{pull}} = 5.4 \text{ mm/h}$  shows a bump around melting point caused by latent heat release which is proportional to growth rate. Jump<sup>2</sup> in derivative around  $z = h + 75 \text{ mm}$  corresponds to jump in heat diffusivity between melt and protective atmosphere on interface  $\Sigma$ .

Experimental values and steady numerical values more or less qualitatively agrees at for temperature profile TP1, TP2 and most of the TP3 measurements. For data of TP3 profile at  $h = 0.2365$  all the measurements including one in figure 4.13a shows a substantial deviation not present to other positions  $h$ . This suggest a possible flaw in these particular measurement. All the experimental data for profile TP4 (see also figures 4.14a, 4.14b) matches very poorly to calculated temperatures.

Sadly, numerical and experimental steady states shows mutual systematic bias up to 20 K. Probable cause is hidden in unrealistic boundary conditions involved. Especially Dirichlet cooling of the holder at 350 K is certainly not realistic and was chosen as the simplest possible realization of the simplest possible temperature measurement method – *one can touch the bottom of the holder by a bare hand*. Also mass and heat insulation at the bottom end of the furnace around the holder is not the case. Hot air is certainly being blown out of the furnace and

---

<sup>1</sup>Note that stationary solution does not depend on pull-rate and time-step – more precisely it corresponds to zero pull-rate in our implementation.

<sup>2</sup>It does not look much as sharp jump on all the figures because plotted data are interpolated to equally distributed nodal values distant 1 mm.

cool air from a room is being sucked in. Modeling and numerical treatment of a problem with pressure-only in/outflows is a challenging task (see for example [43, the Chimney problem]). Other possibility is taking into account broader model involving also some air out of furnace. This could naturally solve also cooling of the holder. On the other hand simple temperature measurements of the holder could save the day.

If we return to the problem with bias and assume that experimental results are correct, we can speculate that an overestimated cooling of the holder could lower temperature in the system globally, thus producing the bias. On the other hand, improper boundary conditions at bottom of the furnace probably have an opposite effect.

We must be critical also to the experiment. At first, layout of the capillaries 1.4 definitely breaks cylindrical symmetry of the system. At second, the capillaries probably influences the measured system. Except for altering velocity field, thermal conductivity of fused quartz is ca. two-times higher than that of both solid and liquid  $\text{PbCl}_2$  but more importantly it is ca. 30-times higher than that of protective atmosphere. Hence added capillaries may cause substantial heat supply or drain in the interior of the ampoule.



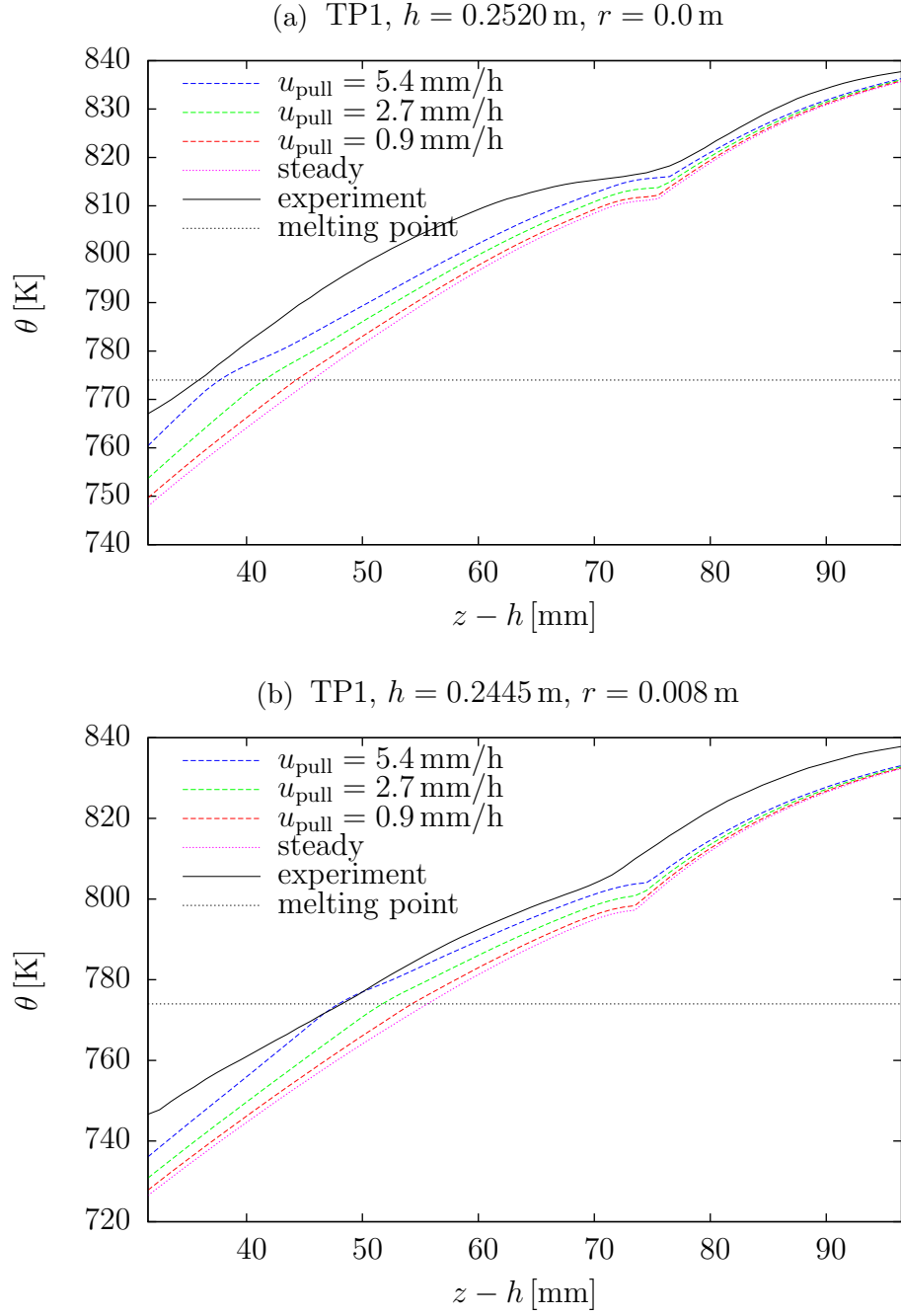


Figure 4.11: Comparison of calculated and measured temperature fields for temperature profile TP1.

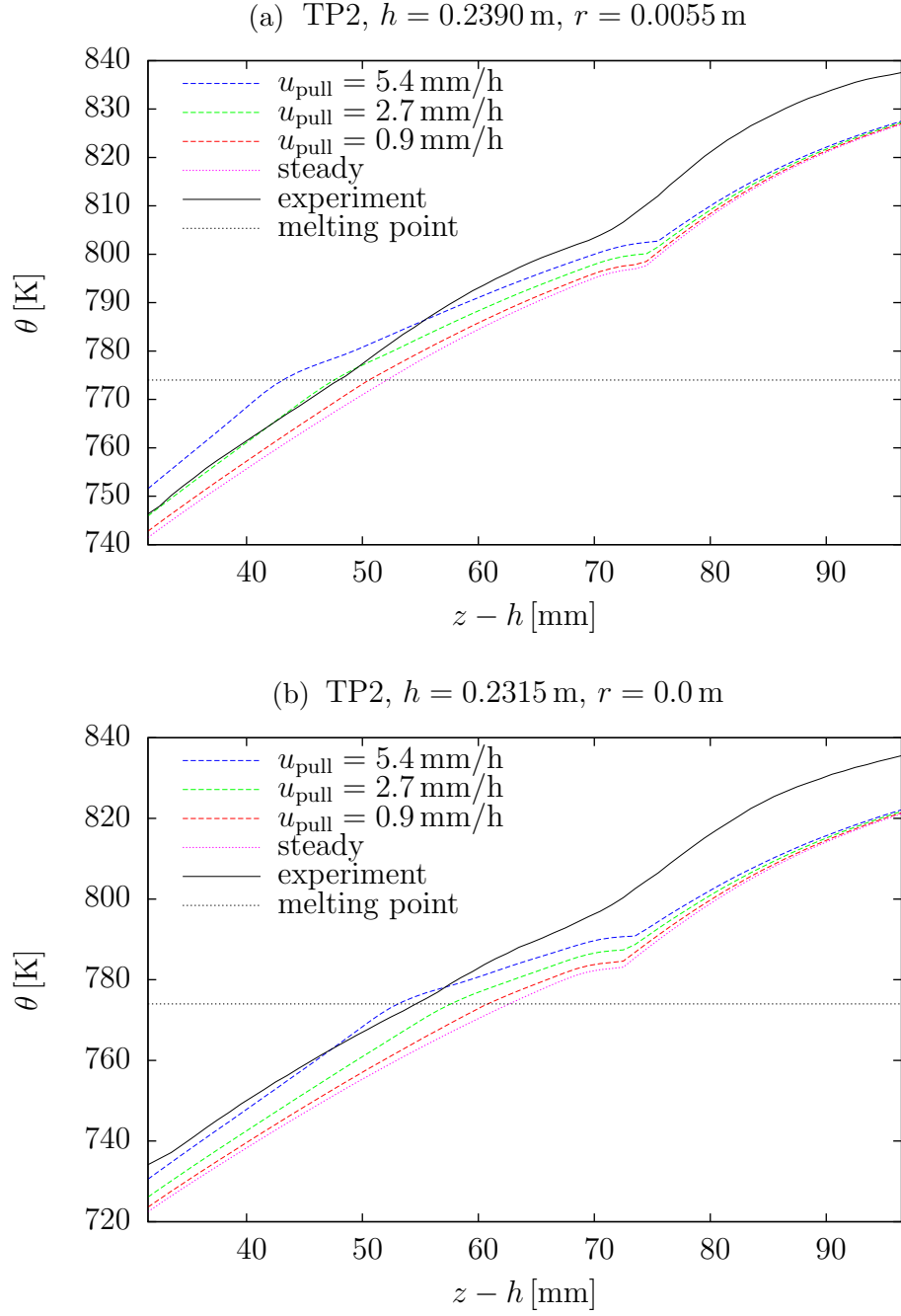


Figure 4.12: Comparison of calculated and measured temperature fields for temperature profile TP2.

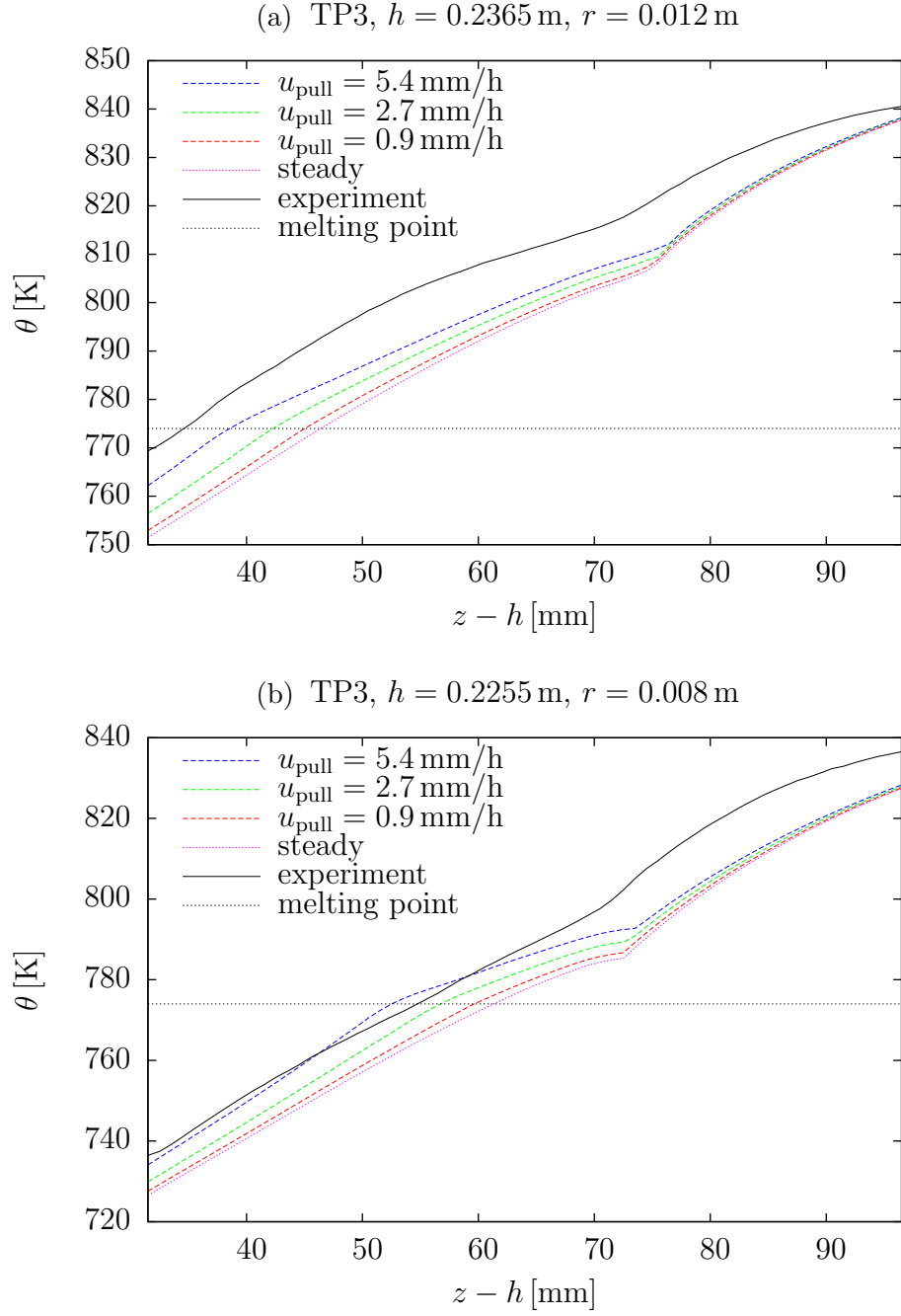


Figure 4.13: Comparison of calculated and measured temperature fields for temperature profile TP3.

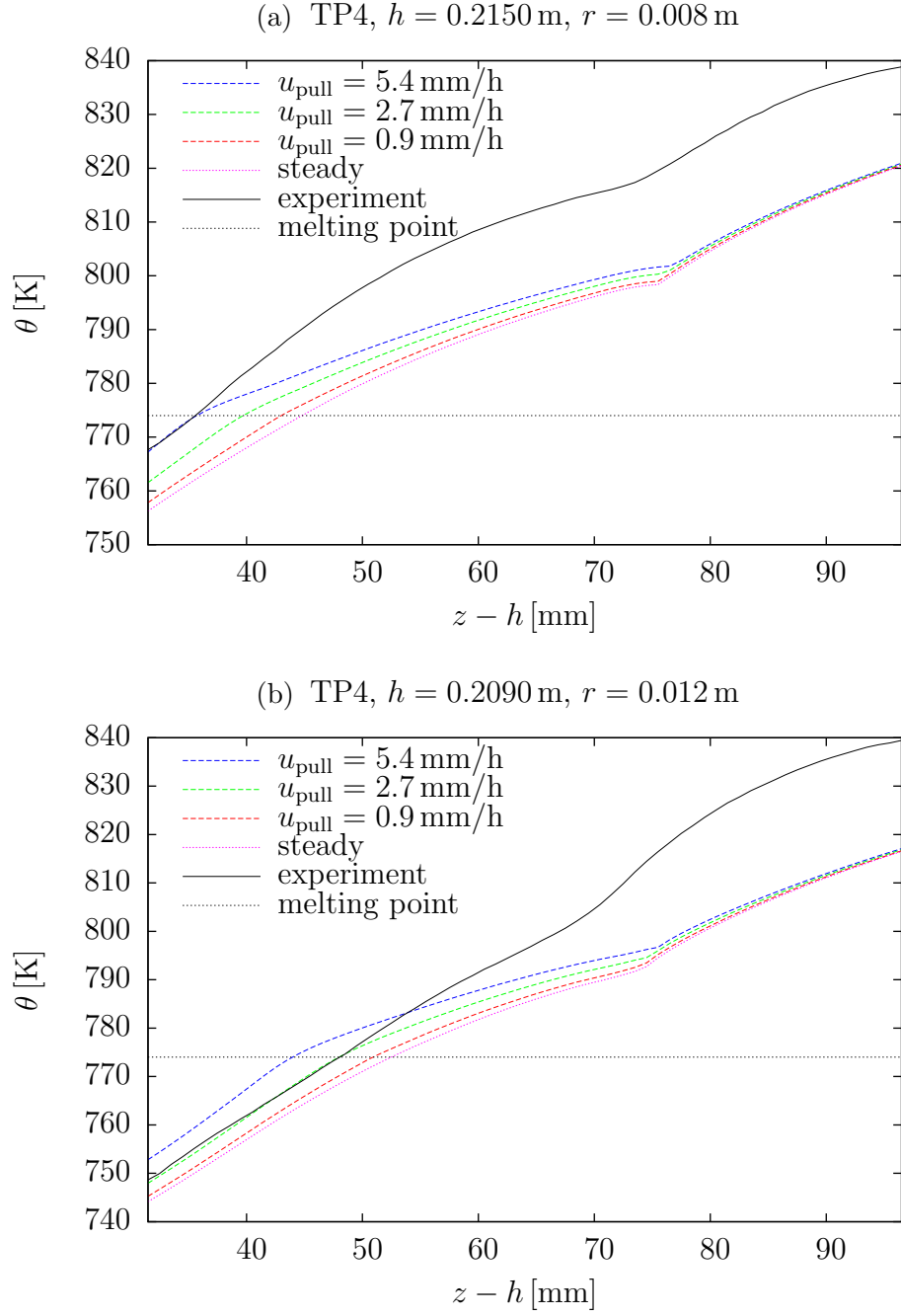


Figure 4.14: Comparison of calculated and measured temperature fields for temperature profile TP4.

# Conclusion

In chapter 2 we considered specific model well-established model of solidification but we advanced in general thermomechanical framework while considering specific demands of our crystal growth problem. In particular we developed a model with ability to handle density jump during phase change. We proceeded by formulating all the specifics of our problem like boundary and interfacial conditions. We reformulated a problem using usual weak formulation and also restated the problem using special weak formulation applicable to axisymmetric problems.

Some of our thoughts regarding recently proposed Allen-Cahn type model [15] were passed. Slight generalization was suggested in order to model be able to describe macroscopic phase transitions driven by temperature or pressure. We were more verbose than [15] in a discussion and a description of used thermodynamical potentials and performing Legendre their transforms. This enabled us to derive Stefan-like enthalpy formulation without unclear assumption [15, equation (3.67)]. Unfortunately we were forced to leave this model due to its problematic applicability to our case.

In chapter 3 we formulated straightforward finite-element discretization of axisymmetric weak problem. Complicated and little unusual is time-discretization because of the mass-conservation demands. We carried out computations using FEniCS which is library for automatic discretization and solution of PDEs using FEM. Therefore we did not need to engage with programming spatial discretization method and we could focus to complicated time-discretization. LU method was used for solution of linear systems. This is very robust but scales poorly. One could proceed with construction of suitable preconditioning algorithm to be able to take advantage of the Krylov methods hence getting ability to solve larger problems.

Finally we presented our numerical results and conclusions in chapter 4. Quantitative analysis of a phase interface shape was not brought to a working state. Results were successfully fitted into anticipated expectations of pull-rate influence on a growth process. We also suggested a possible speed-up of the process by increasing pull-rate when the phase interface is located in conical part of the ampoule. Numerical results were directly compared to temperature data measured on the stationary system. Serious discrepancies were observed. Suggested explanations involve flaws in boundary conditions on the side of a numerical model and possible flaw in the experimental set-up being caused by *a thermometer influencing too much a measured system*.

As a follow-up to this work, some measurements of problematic boundary conditions could be performed on the real system. Conversely numerical model could be tweaked for simulating operation of the *suspected* temperature measurement arrangement. Then accuracy of these measurements could be predicted. This would definitely need a full 3D computation which would probably not be manageable using LU method because of requirements on mesh fineness due to problem stiffness.

# Bibliography

- [1] ALAND, S.; VOIGT, A. *Benchmark computations of diffuse interface models for two-dimensional bubble dynamics*. Int. J. Numer. Meth. Fluids 69 (2012) 747–761.
- [2] ALLEN, S. M.; CAHN, J. W. *Ground State Structures in Ordered Binary Alloys with Second Neighbor Interactions*. Acta Met. 20 (1972) 423.
- [3] AMESTOY, P. R.; DUFF, I. S. and L’EXCELLENT, J.-Y. *Multifrontal parallel distributed symmetric and unsymmetric solvers*. Comput. Methods in Appl. Mech. Eng. 184 (2000) 501–520.
- [4] BALDONI, F.; RAJAGOPAL, K. R. *A Continuum Theory for the Thermomechanics of Solidification*. Int. J. Non-Linear Mechanics 32 (1997) 3–20.
- [5] BECKERMANN, C.; DIEPERS, H.-J.; STEINBACH, I.; KARMA, A.; TONG, X. *Modeling Melt Convection in Phase-Field Simulations of Solidification*. J. Comp. Phys. 154 (1999) 468–496.
- [6] BOYER, F.; LAPUERTA, C. *Study of a three component Cahn-Hilliard flow model*. ESAIM, Math. Model. Numer. Anal. 40 (2006) 653–687.
- [7] BROWN, E. *Mid-infrared emission properties of Nd-doped lead halides for photonic applications*. Mater. Sci. Eng. B 146 (2008) 103–106.
- [8] CAHN, J. W.; HILLIARD, J. E. *Free energy of a nonuniform system. I. Interfacial free energy*. J. Chem. Phys. 28 (1958) 258.
- [9] CHASE, M. W., Jr. *J. Phys. Chem. Ref. Data, Monograph 9: NIST-JANAF Thermochemical Tables*. Fourth Edition, Part I, Al–Co. Woodbury, NY: American Institute of Physics, 1998. ISBN 1-56396-831-2.
- [10] CHessa, J.; SMOLINSKI, P.; BELYTSCHKO, T. *The extended finite element method (XFEM) for solidification problems*. Int. J. Numer. Meth. Engng. 53 (2002) 1959–1977.
- [11] DEPARIS, S. *Numerical Analysis of Axisymmetric Flows and Methods for Fluid-Structure Interaction Arising in Blood Flow Simulation*, PhD thesis. Lausanne: École polytechnique fédérale de Lausanne, 2004.
- [12] DHANARAJ, G.; BYRAPPA, K.; PRASAD, V.; DUDLEY, M. (Eds.) *Handbook of Crystal Growth*. Heidelberg: Springer, 2010. ISBN 978-3-540-74182-4.
- [13] GARAI, J. *Physical model for vaporization*. Fluid Phase Eq. 283 (2009) 89–92.
- [14] GARTLING, D. K. *Finite element analysis of convective heat transfer problems with change of phase*. Computer Methods in Fluids, eds. K. Morgan *et al.* London: Pentech, 1980. p. 257.

- [15] HEIDA, M.; MÁLEK, J.; RAJAGOPAL, K. R. *On the development and generalizations of Cahn-Hilliard equations within a thermodynamic framework.* Z. Angew. Math. Phys. 63 (2012) 145–169.
- [16] —. *On the development and generalizations of Allen–Cahn and Stefan equations within a thermodynamic framework.* Z. Angew. Math. Phys. 63 (2012) 759–776.
- [17] ISAENKO, L. *New Monocrystals with Low Phonon Energy for Mid-IR Lasers.* Chapter in *Mid-Infrared Coherent Sources and Applications.* (Eds. EBRAHIM-ZADEH, M.; SOROKINA, I. T.) Berlin: Springer, 2008.
- [18] JANZ, G. J.; DAMPIER, F. W.; LAKSHMINARAYANAN, G. R.; LORENZ, P. K.; TOMKINS, R. P. T. *Molten Salts: Volume 1, Electrical Conductance, Density, and Viscosity Data.* Washington: United States Department of Commerce, 1968.
- [19] JI, H.; CHOPP, D.; DOLBOW, J. E. *A hybrid extended finite element/level set method for modeling phase transformations.* Int. J. Numer. Meth. Engng. 54 (2002) 1209–1233.
- [20] KRÁL, R. *Study on influence of growth conditions on position and shape of crystal/melt interface of alkali lead halide crystals at Bridgman growth.* J. Crystal Growth 360 (2012) 162–166.
- [21] LOGG, A.; MARDAL, K.-E.; WELLS, G. N. (Eds.) *Automated Solution of Differential Equations by the Finite Element Method.* Heidelberg: Springer, 2012. ISBN 978-3-642-23098-1.
- [22] MARIN, T. L. *Modelling of Free Surface Flow Problems with Phase Change – Three Phase Flows.* Chapter 9 in *Multiphysics Modelling with Finite Element Methods.* (Ed. ZIMMERMAN, W. B. J.) Singapore: World Scientific Publishing Co., 2006.
- [23] MARTYUSHEV, L. M.; SELEZNEV, V. D. *Maximum entropy production principle in physics, chemistry and biology.* Phys. Rep. 426 (2006) 1–45.
- [24] MASSEY, B.; WARD-SMITH, J. *Mechanics of Fluids.* Seventh ed. New York: Spon Press, 1998. ISBN 978-0-7487-4043-7.
- [25] MERLE, R.; DOLBOW, J. *Solving thermal and phase change problems with the eXtended finite element method.* Comp. Mech. 28 (2002) 339–350.
- [26] MORGAN, K. *A numerical analysis of freezing and melting with convection.* Comput. Meth. Appl. Eng. 30 (1987) 1709.
- [27] NITSCH, K. *The purification and preparation of high-purity  $\text{PbCl}_2$  and ternary alkali lead chloride single crystals.* J. Crystal Growth 131 (1993) 612–615.
- [28] —. *Ternary alkali lead chlorides: crystal growth, crystal structure, absorption and emission properties.* Prog. Cryst. Growth Charact. 30 (1995) 1–22.

- [29] PANKRATZ, L. B. *Thermodynamic properties of halides*. Washington: United States Department of the Interior, Bureau of Mines, 1984.
- [30] RADEMAKER, K. *Optical properties of  $Nd^{3+}$ - and  $Tb^{3+}$ -doped  $KPb_2Br_5$  and  $RbPb_2Br_5$  with low nonradiative decay*. J. Opt. Soc. Am. B 21 (2004) 2117–2129.
- [31] RAJAGOPAL, K. R.; RŮŽIČKA, M.; SRINIVASA, A. R. *On the Oberbeck-Boussinesq Approximations*. Math. Models Methods Appl. Sci. 6 (1996) 1157–1167.
- [32] RAJAGOPAL, K. R.; SRINIVASA, A. R. *A thermodynamic framework for rate type fluid models*. J. Non-Newtonian Fluid Mech. 88 (2000) 207–227.
- [33] —. *On the thermomechanics of materials that have multiple natural configurations. Part I: Viscoelasticity and classical plasticity* Z. Angew. Math. Phys. 55 (2004) 861–893.
- [34] ROBIE, R. A.; HEMINGWAY, B. S. *Thermodynamic Properties of Minerals and Related Substances at 298.15 K and 1 Bar ( $10^5$  Pascals) Pressure and at a Higher Temperatures*. Washington: United States Government Printing Office, 1995.
- [35] RODOVÁ, M. *Measurement of linear expansion coefficient of  $PbCl_2$* . Unpublished preprint. Prague: Institute of Physics, Department of Optical Materials, 2013.
- [36] SHEWCHUK, J. R. *Triangle: Engineering a 2D Quality Mesh Generator and Delaunay Triangulator*. Applied Computational Geometry: Towards Geometric Engineering (Eds. LIN, M. C.; MANOCHA, D.) 203–222. Berlin: Springer, 1996.
- [37] —. *Delaunay Refinement Algorithms for Triangular Mesh Generation*. Comp. Geom. Theory Appl. 22 (2002) 21–74.
- [38] —. *What Is a Good Linear Finite Element? Interpolation, Conditioning, Anisotropy, and Quality Measures*. Unpublished preprint. Berkeley, CA: University of California at Berkeley, 2002. Available online at <http://www.cs.berkeley.edu/~jrs/papers/elemj.pdf>.
- [39] SHYY, W.; CHEN, M.-H. *Steady-state natural convection with phase change*. Int. J. Heat Mass Transfer 33 (1990) 2545.
- [40] SHYY, W.; OUYANG, H. *Numerical simulation of CdTe vertical Bridgman growth*. J. Cryst. Growth 173 (1997) 352–366.
- [41] ŠILHAVÝ, M. *The Mechanics and Thermodynamics of Continuous Media*. Berlin: Springer, 1997. ISBN 3-540-58378-5.
- [42] VOLLER, V. R.; PRAKASH, C. *A fixed grid numerical modelling methodology for convection-diffusion mushy region phase-change problems*. Int. J. Heat Mass Transfer 30 (1987) 1709.



- [43] WESSELING, P. *Principles of Computational Fluid Dynamics*. Berlin: Springer, 2001.
- [44] WIKIPEDIA, The Free Encyclopedia. *Fused quartz*. Available online at [http://en.wikipedia.org/w/index.php?title=Fused\\_quartz&oldid=565476741](http://en.wikipedia.org/w/index.php?title=Fused_quartz&oldid=565476741).
- [45] WIKIPEDIA, The Free Encyclopedia. *Grüneisen parameter*. Available online at [http://en.wikipedia.org/w/index.php?title=Gr%C3%BCneisen\\_parameter&oldid=550906704](http://en.wikipedia.org/w/index.php?title=Gr%C3%BCneisen_parameter&oldid=550906704).
- [46] WIKIPEDIA, The Free Encyclopedia. *Chlorid olovnatý (Lead(II) chloride)*. Available online at [http://cs.wikipedia.org/w/index.php?title=Chlorid\\_olovnat%C3%BD&oldid=10442609](http://cs.wikipedia.org/w/index.php?title=Chlorid_olovnat%C3%BD&oldid=10442609).
- [47] WIKIPEDIA, The Free Encyclopedia. *Lead(II) chloride*. Available online at [http://en.wikipedia.org/w/index.php?title=Lead\(II\)\\_chloride&oldid=552080584](http://en.wikipedia.org/w/index.php?title=Lead(II)_chloride&oldid=552080584).

# List of tables

2.1	Used values of material coefficients. . . . .	17
4.1	Used numerical parameters. . . . .	33
4.2	Used initial values $h^0$ of ampoule position $h$ . . . . .	34

# List of abbreviations and symbols

## Abbreviations (alphabetically)

ALE – arbitrary Lagrangian–Eulerian	PDE – partial differential equation
FEM – finite element method	PUM – partition of unity method
FFC – FEniCS Form Compiler	RE – rare earth (element)
MPI – Message Passing Interface	TALH – ternary alkali lead halides
MUMPS – MULTifrontal Massively Parallel sparse direct Solver	XFEM – extended finite element method

## Symbols (in order of appearance)

$\rho$ – density	$c_p^{\text{eff}}$ – effective heat capacity including latent heat as (approximate) Dirac- $\delta$ distribution
$\mathbf{u}$ – velocity	
$p$ – pressure	$\kappa$ – thermal conductivity
$\mathbf{T}$ – Cauchy stress	$\mu$ – viscosity
$\mathbf{b}$ – (volumetric) body force	$S$ – Darcy like forcing enforcing no- flow in solid phase
$e$ – internal energy	$\mathbf{g}$ – gravity acceleration due to Earth
$\mathbf{q}$ – heat flux	$C$ – parameter of forcing $S$
$\mathbf{S}$ – dissipative part of the Cauchy stress	$\phi$ – porosity
$\nu = 1/\rho$ – specific mass	$\Omega$ – domain occupied by $\text{PbCl}_2$
$h = e + p\nu$ – enthalpy	$\Lambda$ – domain occupied by protective at- mosphere
$0 \leq c \leq 1$ – phase-field variable	$\Sigma = \partial\Omega \cap \partial\Lambda$
$\eta$ – entropy	$u_z = U$ – vertical (aligned with gravi- ty) component of $\mathbf{u}$
$\mu$ – chemical potential	$\alpha_\Omega, \alpha_\Lambda, \alpha$ – approximation of $-\rho'$ in pseudo-compressibility constraint
$c_p$ – heat capacity at constant pressure	$\Delta$ – domain occupied by air
$L$ – latent heat of phase change	$\Phi$ – domain occupied by ampoule
$\alpha$ – thermal expansion coefficient	$\Psi$ – domain occupied by holder
$\epsilon$ – temperature range of diffuse inter- face	$\mathbf{u}_{\text{pull}}$ – pull-rate of holder with ampoule

$\mathbf{n}, \tau$ – normal and tangential unit vector of respective surface	$\sigma$ – surface tension/energy
$\hat{\Omega}, \hat{\Lambda}, \hat{\Delta}, \hat{\Phi}, \hat{\Psi}$ – 3D counterparts of respective domains	$f, f^B, f_\epsilon^I$ – Helmholtz free energy and its bulk and interfacial part
$H^1$ – Sobolev space of square-integrable functions with square-integrable derivatives	$F$ – free energy functional
$L^2$ – Lebesgue space of square-integrable functions	$\phi, \psi, D$ – general unknown, test function and domain in context of ALE framework
$\hat{V}, \hat{P}, \hat{Q}$ – 3D function space for velocity, pressure and temperature	$\mathbf{u}^B$ – reference-frame velocity, velocity of domain boundaries and mesh
$\mathbf{u}^D, \theta^D$ – representants of velocity and temperature Dirichlet condition	$\frac{D^B}{Dt}$ – $\mathbf{u}^B$ -based convective derivative
$\mathbf{v}, q, \eta$ – general test functions from some velocity, pressure and temperature space	$\phi = \phi_i(t)\phi^i(x, t)$ – Galerkin expansion by $\mathbf{u}^B$ -convected basis
$L^\infty$ – Lebesgue space of essentially bounded functions	$\mathcal{T}_h, T$ – triangulation and its triangle
$x, y, z$ – Cartesian coordinates	$\mathbf{u}_h, p_h, \theta_h$ – FEM approximations of velocity, pressure and temperature
$r, \varphi, z$ – cylindrical coordinates	$\Gamma_{\mathbf{u}}^D, \Gamma_\theta^D$ – Dirichet surfaces of velocity and temperature
$\hat{\mathbf{r}}, \hat{\varphi}, \hat{\mathbf{z}}$ – unit coordinate vectors of cylindrical coordinate system	$\mathcal{C}$ – space of continuous functions
$u_r, u_z$ – respective components in cylindrical basis of arbitrary vector $\mathbf{u}$	$\mathcal{P}_n$ – space of polynomials up to degree $n$
$L_\alpha^p$ – weighted Sobolev space of square-integrable functions with weight $r^\alpha$	$q$ – parameter of modified Darcy term
$H_1^1$ – weighted Sobolev space induced by $L_1^1$	$\delta t, t^n = n \delta t$ – time-step and time-levels
$V_1^1 = H_1^1 \cap L_{-1}^2$	$\phi^n$ – approximation of $\phi$ at $t^n$
$V_r, V_z, P, Q$ – function spaces for radial and axial velocity, pressure and temperature appropriate for axial-symmetry	$\frac{\delta^B}{\delta t}$ – backward-Euler approximation of $\frac{D^B}{Dt}$
	$\hat{\rho}^n$ – density on mesh adjusted subject to mass-conservation
	$m_{\text{PbCl}_2}^0$ – total mass of $\text{PbCl}_2$
	$\mathbf{d}^n$ – displacement of mesh